Growth and characterization of single crystals of oxide based solid electrolyte for application of all solid-state Li-ion batteries

(全固体リチウムイオン電池への応用を目指した酸化物系固体電解質の単結晶の育成と評価)

PhD Dissertation

Integrated Graduate School of Medicine, Engineering and Agricultural Sciences

University of Yamanashi, Japan

September 2023

Most. Umme Salma

Dedicated

To My Respectable Parents

Declaration

I hereby declare that the entire research work embodied in this thesis entitled "Growth and characterization of single crystals of oxide based solid electrolyte for application of all solid-state Li-ion batteries" has been accepted to the faculty of Integrated Graduate School of Medicine, Engineering and Agricultural Sciences, University of Yamanashi, Japan for the PhD degree. This thesis is written by myself and has not been submitted to any other academic institution for any degree or award.

Part of this thesis have been published, as listed as below:

1. **Most. Umme Salma**, Yuki Maruyama, Masanori Nagao, Satoshi Watauchi, Hirokazu Munakata, Kiyoshi Kanamura and Isao Tanaka, "TSFZ growth and anisotropic ionic conductivity of $Li_xLa_{(1-x)/3}TaO_3$ single crystals", *Journal of the Ceramic Society of Japan* **131 [4]** 72-76 (2023).
2. **Most. Umme Salma**, Md. Shahajan Ali, Yuki Maruyama, Masanori Nagao, Satoshi Watauchi and Isao Tanaka, "Growth of Large-diameter $Li_xLa_{(1-x)/3}NbO_3$ Single Crystal by the TSFZ method using a tilting-mirror FZ furnace", *Journal of Flux Growth* **17 [1]** 7-11 (2023).

Most. Umme Salma

September 2023

Certificate

*I hereby certify that the thesis entitled "**Growth and characterization of single crystals of oxide based solid electrolyte for application of all solid-state Li-ion batteries**" submitted by Most. Umme Salma, Student Registration No.: G20DTEA4, has been completed under my direct supervision.*

This is bona fide record of the research carried out by the candidate. To the best of my knowledge, this thesis has not been submitted for the award of any degree or award elsewhere.

Supervisor

Professor Nobuhiro Kumada

Center for Crystal Science and Technology

University of Yamanashi

Miyamae 7-32, Kofu, Yamanashi 400-0021, Japan

Phone (+81)55-220-8615

Fax (+81)55-220-8270

Mail: kumada@yamanashi.ac.jp

A B S T R A C T

In this study, single crystals of double-perovskite-type oxide $Li_xLa_{(1-x)/3}TaO_3$ (LLTaO) were successfully grown using the traveling solvent floating zone (TSFZ) method. The Ta-rich phase, which was precipitated in the crystals, was grown via the conventional floating zone (FZ) growth process, indicating that LLTaO behaved as an incongruent melt. For the TSFZ growth for solvents with a $LiTa_3O_8$ composition of 8%, which is less than the LLTaO (x = 0.18) stoichiometric composition, the black grown crystals were homogeneous and crack-free, with a typical size of approximately 20 mm in length and 5 mm in diameter. The grown crystals turned colorless and transparent after being left overnight in the air at room temperature (about 25 °C). The Li concentration in the grown crystals was determined to be x = 0.086(1). This value is lower than the nominal composition (x = 0.18) of the feed owing to Li evaporation during the crystal growth. The ionic conductivities of the grown crystals along [110] and [001] were 2.8×10^{-5} and 1.8×10^{-5} $S\cdot cm^{-1}$, respectively. The anisotropic parameter was determined to be 1.56 indicating that the ionic conductivity along the *ab*-plane is higher than that along the *c*-axis. Furthermore, the calculated activation energies along [110] and [001] were 0.29 and 0.34 eV, respectively.

Large diameter single crystals of $Li_xLa_{(1-x)/3}NbO_3$ with a Li concentration of x = 0.10 were grown by using the traveling solvent floating zone (TSFZ) method. A tilting-mirror FZ furnace with θ = 10° mirror tilt angle was the best choice to grow high-quality single crystal of $Li_xLa_{(1-x)/3}NbO_3$. The required lamp power and convexity were lower for the tilting-mirror FZ furnace than for the conventional FZ furnace. The convexity of the

crystal-liquid interface was low in the case of a $\theta = 10°$ mirror tilt angle. Due to the low lamp power required, little Li evaporated in the tilting-mirror FZ furnace with $\theta = 10°$, which was observed in the quartz tube and EPMA analysis.

CONTENTS

Chapter 3

Chapter 4

Chapter 5

Chapter 6

APENDIX

Chapter 1

General introduction

1.1. Lithium-ion battery and solid-state lithium-ion battery

Undesirable climate change and environmental destruction is one of the greatest challenges to humankind. The increasing global consumption of fossil fuels leading to increase the levels of CO_2 which plays a big role to the climate change in our atmosphere [1-4]. Therefore, it is crucial to develop renewable energy storage and conversion to meet these challenges [5-8]. Among the available energy conversion and storage technologies, lithium-ion batteries (LIBs) play an important role due to their advantages such as high specific energy, high energy density, long cycle life, low self-discharge rate, and light weight. LIBs have revolutionized our daily lives since their commercialization in 1991 [9]. In addition, the scientists, John B. Goodenough (The University of Texas at Austin, USA), M. Stanley Whittingham (Binghamton University, State University of New York, USA) and Akira Yoshino (Asahi Kasei Corporation, Tokyo, Japan, & Meijo University, Nagoya, Japan) won the Noble prize in chemistry in 2019 for their contributions to the development of the LIBs [10]. The production of LIBs has been continually increasing day by day for various application sectors including portable electronic devices, electric/hybrid electric vehicles, marine vehicles, autonomous aircraft, smart grids, solar power storage systems, robots etc. [11-19]. The applications of LIBs in various sectors are shown in **Fig 1.1** [20]. For example, the expected demand of LIBs for global market is undergoing an enormous growth from 259 to 2500 GWh within the years of 2020 to 2030 (increasing by an average of 25.4% year) [21-22] whereas from 10 GWh in 2015 to almost 1300 GWh in 2030 for only electric mobility applications [23].

Fig. 1.1. Applications of Li-ion batteries [20].

However, there is some drawback of traditionally used LIBs. In traditionally used LIBs, organic liquids are used as electrolyte. But high voltages do not allow to use aqueous solutions as the electrolyte because the cell voltage exceeds the decomposition voltage of water. Therefore, flammable organic liquid electrolytes cause safety concerns in LIBs. In addition, recent environmental concerns have increased the demand of large-sized batteries for power vehicles [24]. Hence, the increasing battery size increases the amount of combustible electrolyte which may causes to easily heat up toward thermal runaway. For these, the increasing battery size also makes the safety issues more serious [25]. For example, in 2013 a Japan airline 787 Dreamliner's cargo and in 2016 Samsung's Galaxy

note 7 catching on fire [26-28]. This firing problems might be occurred due to the leakage of the organic liquid electrolyte which caused short circuit in LIBs. Hence, development of LIBs is a very crucial task for next generation energy storage devices. To prevent the dendrite formation, replacement of solid electrolyte instead of flammable liquid electrolyte may play an important role for the next generation [29-31]. Hence, Solid-state LIBs become a good alternative to LIBs. In all solid-state LIBs, there is no liquid electrolytes which also reduces the size of the batteries. **Fig. 1.2** shows the configuration conventional LIBs and solid-state LIBs.

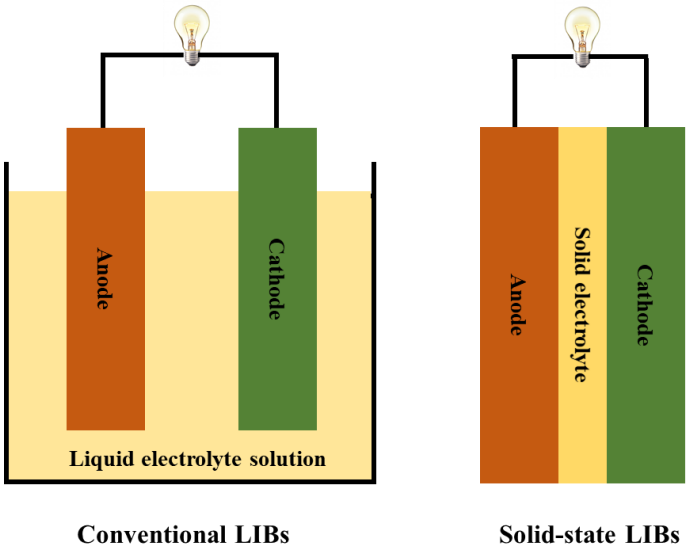

Fig. 1.2. Configuration conventional LIBs and solid-state LIBs.

In 1980s, solid-state LIBs with solid electrolytes instead of liquid electrolytes and separators in traditional LIBs were reported before the successfully commercialization of LIBs [32]. Solid electrolytes, as opposed to flammable liquid electrolytes, can significantly reduce the safety concern of rechargeable batteries. For instance, inorganic solid electrolytes have a fire hazard onset temperature of several hundred degrees Celsius,

whereas liquid electrolytes are invariably already on fire at this temperature [33]. In addition, solid-state LIBs show better chemical and electrochemical stabilities, higher energy density than that of traditional LIBs [34-35]. Hence, Solid-state LIBs process various advantages than that of traditional LIBs as shown in **Fig. 1.3.**

Fig. 1.3. Advantages of solid-state LIBs [35].

1.2. Solid electrolytes

Solid-state electrolytes or solid electrolytes are solid-state ionic conductors and electronic insulating materials. At room temperature solid electrolytes are solid and the ionic movement occurs at the solid-state. It is an important component for all solid-state Li-ion batteries (LIBs). Now a days, research on solid electrolytes have attracted enormous attention for developing all solid-state LIBs due to their various advantages including absolute safety, no issues of leakages of toxic organic solvents, low flammability, non-

volatility and higher cyclability [36]. However, some several basic requirements are needed for solid electrolyte to use in solid-state LIBs [37-39]:

1. High ionic conductivity (more than 10^{-4} S cm^{-1} at room temperature).

2. Low electric conductivity (less than 10^{-10} S cm^{-1} to avoid short circuit inside the battery) with high ionic transference number.

3. Low interface impedance with electrodes.

4. Good chemical and electrochemical stability windows.

5. Strong mechanical strength and good compatibility with electrode materials.

6. Easy processing.

7. Low in cost.

All solid-state electrolytes are divided into three main categories including solid polymer electrolyte, inorganic solid electrolyte and composite polymer electrolyte. Solid polymer electrolytes have good chemical stability and mechanical flexibility. However, the solid polymer electrolytes have a severe flammability limit and low ionic conductivity. Besides, an inorganic solid electrolyte is a specific type of all-solid electrolyte that consists of an inorganic material in a crystalline or glassy state and conducts ions by diffusion through a lattice. Now a days, a large number of inorganic solid electrolytes have been extensively studied because of their exceptional properties including innate incombustibility and non-volatility, high ionic conductivity (>0.1 m S cm^{-1} at room-temperature) close-to-unity, high modulus (or example, >1 G Pa for oxides), excellent thermal stability (stable above 100°C), wide and high electrochemical-stability windows and high transfer ionic number compared to others solid electrolytes [40-43]. Inorganic solid electrolytes including sulfides, glasses or oxides may expected as electrolytes for the next generation LIBs. Glasses and sulfides have high ionic conductivity but these are air exposure and produce

environmentally toxic hydrogen sulfide. In addition, solid sulfides may react with lithium metal anode and cause short circuit problem in LIBs [44-49]. Several types of oxide solid electrolytes are introduced such as NASICON-type ($Na_{1+x}Zr_2Si_xP_{3-x}O_{12}$) [50], Garnet-type ($Li_7La_3Zr_2O_{12}$) [51], LISICON-type ($Li_{3.5}Si_{0.5}P_{0.5}O_4$) [52] and Perovskite-type ($Li_xLa_{(1-x)/3}TiO_3$) [53] solid electrolyte. Compared to others solid electrolytes, Perovskite-type oxide electrolytes are environmentally safe in use, have high ionic conductivity (for example, LLTiO), high chemical and mechanical stability window. However, the double perovskite tetragonal crystal structure (for examples, $Li_xLa_{(1-x)/3}MO_3$, M = Ti, Nb, Ta) shows the anisotropic ionic conductivity [54]. However, Ti^{4+} can be easily reduced by Li-metal anode, producing Ti^{3+} in higher-capacity LIBs applications [55-61]. In contrast, Nb^{5+} and Ta^{5+} is resistant to reduction by Li-metal anode. Therefore, $Li_xLa_{(1-x)/3}TaO_3$ (LLTaO) and $Li_xLa_{(1-x)/3}NbO_3$ (LLNbO) with a double-perovskite structure is a desirable solid electrolyte candidate for investigating high-capacity LIBs. However, grain boundaries and random crystallographic orientation in polycrystalline decrease its ionic conductivity. In addition, dendrite may be created from anode to cathode through polycrystalline electrolytes. In contrast, single crystal of solid electrolyte possesses unique properties due to their continuous, uniform and highly-ordered structure. However, single crystals have no void or grain boundary. For these, there is also no chance of dendrite formation from anode to cathode and thereby increase the lifetime and safety issues of LIBs [62-64]. So, research on single crystal of double-perovskite oxide solid electrolytes (LLTaO and LLNbO) is very important for developing the all solid-state LIBs.

1.3. Purpose of this research

For the development of all solid-state Li-ion batteries (LIBs), research on single crystal of solid electrolyte is important in this present era. LIBs may cause firing or explosion problem due to dendrite formation from anode to cathode by using liquid or polymer-based electrolytes. However, polycrystalline solid electrolytes contain grain boundary which reduces the ionic conductivity and also cases the dendrite formation from anode to cathode. So, it is urgent needed to find out the suitable solid electrolyte for the practical application of all solid-state LIBs. To the best of our knowledge, there is no report on $Li_xLa_{(1-x)/3}TaO_3$ (LLTaO) single crystals. Besides, there is some report on small diameter $Li_xLa_{(1-x)/3}NbO_3$ (LLNbO) single crystals. But large diameter LLNbO single crystals are needed for practical applications of all solid-state LIBs. So, my research purpose is to grow high quality, crack- and inclusion-free single crystals growth of solid electrolytes LLTaO and large diameter LLNbO using TSFZ method for the first time and also their characterization.

In this study, single crystals of LLTaO and LLNbO were grown using traveling solvent floating zone (TSFZ) method. The TSFZ method, which uses solvents, is an extensive crystal-growth technique for incongruent-melting compounds. In addition, as the growth temperature can be lowered by the solvent, the TSFZ method is expected to reduce the evaporation of the Li component from the melt. However, the grown crystals using TSFZ method are large in size.

References

1) S. D. Ebbesen, R. Knibbe and M. Mogensen, *J. Electrochem. Soc.*, **159** F482 (2012).
2) H. Zhang, C. Li, M. Piszcz, E. Coya, T. Rojo, L. M. Rodriguez-Martinez, M. Armand and Z. Zhou, *Chem. Soc. Rev.*, **46** 797 (2017).
3) Y. Zheng, J. Wang, B. Yu, W. Zhang, J. Chen, J. Qiao and J. Zhang, *Chem. Soc. Rev.* **46** 1427 (2017).
4) Y. Zheng, W. Zhang, Y. Li, J. Chen, B. Yu, J. Wang, L. Zhang and J. Zhang, *Nano Energy* **40** 512 (2017).
5) E. Pomerantseva, F. Bonaccorso, X. Feng, Y. Cui and Y. Gogotsi, *Science* **366** 8285 (2020).
6) Q. Zheng, Y. Yamada, R. Shang, S. Ko, Y. Y. Lee, K. Kim, E. Nakamura and A. Yamada, *Nat. Energy* **5** 291 (2020).
7) Zhao, S. Stalin, C. Z. Zhao and L. A. Archer, *Nat. Rev. Mater.* **5** 229 (2020).
8) Y. Zheng, C. Zhao, Y. Li, W. Zhang, T. Wu, Z. Wang, Z. Li, J. Chen, J. Wang, B. Yu and J. Zhang, *Nano Energy* **78** 105236 (2020).
9) Z. Ogumi, R. Kostecki, D. Guyomard and M. Inaba, *Electrochem. Soc. Interface* **25** 65 (2016).
10) C. Thies, K. Kieckhäfer, T. S. Spengler and M. S. Sodhi, *Procedia CIRP* **80** 292 (2019).
11) J. -M. Tarascon and M. Armand, *Nature* **414** 359 (2001).
12) A. S. Arico, P. Bruce, B. Scrosati, J.-M. Tarascon and W. Van Schalkwijk, *Nat. Mater.* **4** 366 (2005).
13) M. Armand and J.-M. Tarascon, *Nature* **451** 652 (2008).

14) P. G. Bruce, B. Scrosati, and J.-M. Tarascon, *Angew. Chem. Int. Ed.* **47** 2930 (2008).

15) J. B. Goodenough and Y. Kim, *Chem. Mater.* **22** 587 (2010).

16) V. Etacheri, R. Marom, R. Elazari, G. Salitra and D. Aurbach, *Energy Environ. Sci.* **4** 3243 (2011).

17) B. Dunn, H. Kamath and J.-M. Tarascon, *Science* **334** 928 (2011).

18) N. Nitta, F. Wu, J.T. Lee and G. Yushin, *Mater. Today* **18** 252 (2015).

19) J. W. Choi and D. Aurbach, *Nat*. *Rev*. *Mater*. **1** 16013 (2016).

20) https://www.pasticheenergysolutions.com/applications/

21) E. Fan, L. Li, Z. Wang, J. Lin, Y. Huang, Y. Yao, R. Chen and F. Wu, *Chem. Rev.* **120** 7020 (2020).

22) H. E. Melin, M. A. Rajaeifar, A. Y. Ku, A. Kendall, G. Harper and O. Heidrich, *Science* **373** 384 (2021).

23) A. Dixit, Department of Physics & Center for Solar Energy, Indian Institute of Technology Jodhpur, Jodhpur 342037, India, Cathode Materials for Lithium Ion Batteries (LIBs): A Review on Materials related aspects towards High Energy Density LIBs.

24) M. Armand, J. M. Tarascon, *Nature* **451** 652 (2008).

25) W. Li, J. R. Dahn, and D. S. Wainwright, *Science* **264** 1115(1994)

26) "Dreamliner: Boeing 787 planes grounded on safety fears" BBC News, January 17, 2013.

27) A. Burning, *Chem. Eng. News* **94 (45)** 33 (2016).

28) S. Boyford, Samsungs says bad batteries and rushed manufacturing doomed the Galaxy Note 7, January 22, 2017.

29) J. Zhang, W. Xu and W. A. Henderson, *Springer International Publishing* **7** 153 (2016).

30) J. Newman and C. Monroe, *J. Electrochem. Soc.* **150 (10)** A1377 (2003).

31) K. J. Harry, "Lithium dendrite growth through solid polymer electrolyte membranes. United States: N. p., 2016.

32) J.-F. Wu, R. Zhang, Q.-F. Fu, J.-S. Zhang, X.-Y. Zhou, P. Gao, C.-H. Xu, J. Liu and X. Guo, *Adv. Funct. Mater.* **31** 2008165 (2021).

33) R. Chen, Q. Li, X. Yu, L. Chen and H. Li, *Chem. Rev.* **120** 6820 (2019).

34) J. Li, C. Ma, M. Chi, C. Liang and N. J. Dudney, *Adv. Energy Mater.* **5** 1401408 (2014).

35) A. Arya and A. L. Sharma, *J. Mater. Sci.* **55** 44 (2020).

36) Z. Chena, G.-T. Kima, Z. Wangd, D. Bressera, B. Qina, D. Geigere, U. Kaisere, X Wangd, Z. X. Shenc and S. Passerini, *Nano Energy* **64** (2019)103986.

37) V. T. R. Murugan and W. Weppner, *Angew. Chem. Int. Ed.* **46** 7778 (2007).

38) R. Chen, A. M. Nolan, J. Lu, J. Wang, X. Yu, Y. Mo, L. Chen, X. Huang and H. Li, *Joule* **4** 812 (2020).

39) F. Zheng, M. Kotobuki, S. Song, M. O. Lai and L. Lu, *J. Power Sources* **389** 198 (2018).

40) Q. Zhao, S. Stalin, C.-Z. Zhao and L. A. Archer, *Nat. Rev. Mater.* **5** (3) 229 (2020).

41) A. Manthiram, X. W. Yu and S. F. Wang, *Nat. Rev. Mater.* **2** 16103 (2017).

42) M. S. Reisch, *Chem. Eng. News* **95 (46)** 19 (2017).

43) X. Wu, K. Pan, M. Jia, Y. Ren, H. He, L. Zhang and S. Zhang, *Green Energy & Environment* **4** 360 (2019).

44) N. Kamaya, K. Homma, Y. Yamakawa, M. Hirayama, R. Kanno, M. Yonemura, T. Kamiyama, Y. Kato, S. Hama, K. Kawamoto and A. Mitsui, *Nat. Mater.* **10** 682 (2011).

45) F. Aguesse, V. Roddatis, J. Roqueta, P. Garcia, D. Pergolesi, J. Santiso and J. A. Kilner, *Solid State Ionics* **272** 1 (2015).

46) D. Rettenwander, R. Wagner, J. Langer, M. E. Maier, M. Wilkening and G. Amthauer, *Eur. J. Mineral.* **28** 619 (2016).

47) K. Kataoka, H. Nagata and J. Akimoto, *Sci. Rep.* **8** 9965 (2018).

48) S. Minegishi, T. Hoshina, T. Tsurumi, K. Lebbou and H. Takeda, *J. Ceram. Soc. Japan* **128** 481 (2020).

49) M. A. R. Sarker, S. Watauchi, M. Nagao, M. M. Hossain and I. Tanaka, *J. Phys.: Conf. Ser*. **1718** 012012 (2021).

50) C. J. Leo, G. V. S. Rao and B. V. R. Chowdari, *J. Mater. Chem.* **12** 1848 (2002).

51) C.-. Tsai, V. Roddatis, C. V. Chandran, Q. Ma, S. Uhlenbruck, M. Bram, P. Heitjans., and O. Guillon, *ACS Appl. Mater. Interfaces* **8** 10617 (2016).

52) S. Woo and B. Kang *J. Mater. Chem. A* **10** 23185 (2022).

53) Y. Inaguma, C. Liquan, M. Itoh, T. Nakamura, T. Uchida, H. Ikuta and M. Wakihara, *Solid State Commun.* **86** 689 (1993).

54) Y. Maruyama, S. Minamimure, C. Kobayashi, M. Nagao, S. Watauchi and I. Tanaka, *R. Soc. Open Sci.* **5** 181445 (2018).

55) K. Mizumoto and S. Hayashi, *Solid State Ionics* **116** 263 (1999).

56) C. Y. Sun and K. Z. Fung, *Solid State Commun.* **123** 431 (2002).

57) S. Stramare, V. Thangadurai and W. Weppner, *Chem. Mater.* **15** 3974 (2003).

58) M. Vijayakumar, J. Emery, O. Bohnke, R. L. Vold and G. L. Hoatson, *Solid State*

Ionics **177** 1673 (2006).

59) P. Knauth, *Solid State Ionics* **180** 911 **(**2009).

60) K. K. Bharathi, H. Tan, S. Takeuchi, L. Meshi, H. Shen, J. Shin, I. Takeuchi and L. A. Bendersky, *RSC Adv.* **6** 61974 (2016).

61) R. Yu, Q. -X. Du, B. -K. Zou, Z. -Y. Wen and C. -H. Chen, *J. Power Sources* **306** 623 (2016).

62) K. Kataoka, H. Nagata and J. Akimoto, *Sci. Rep.* **8** 9965 (2018).

63) M. A. R. Sarker, S. Watauchi, M. Nagao, M. M. Hossain and I. Tanaka, *J. Phys. Conf. Ser.* **1718** 012012 (2021).

64) E. D. Barr, *Contemporary Physics* **2** 409 (1961).

Chapter 2

Overview of Experimental Procedure

2.1. Morphology of crystal growth processes

2.1.1. Floating Zone (FZ) and Travelling Solvent Floating Zone (TSFZ) Methods

The FZ method is a very popular method for the single crystal growth. **Fig. 2.1** shows the schematic view of this method. The molten zone is maintained between two vertical solid rods; polycrystalline feed rod and seed crystal during FZ formation by its own surface tension. The single crystal growth is performed by dipping a seed crystal into one end of the zone and moving the molten zone in the direction of the feed stock. The upper end of the feed rod is clamped vertically by a holder to the upper pulling shaft and the other end is tapered and heated to melting its tip. Heating of the molten zone can be done by several methods such as RF coil (inductor), optical, electron beam, laser and resistance heating. The trip of the feed is properly melted and then formed a drop which contacted with the oriented seed crystal to the lower pulling shaft. When solid/melt contact becomes stable, the seed and the feed rods are concurrently moved downward to maintain stable molten zone in correspondence with the fixed heater and to crystallize a single crystal. The seed crystal and the feed rod are rotated to get cylindrical ingots. However, using different speeds for feed rod and seed crystal, it can be obtained larger or smaller diameter crystal than that of the starting feed rod by pressing or stretching the molten zone respectively [1-6].

For congruently melting materials, the composition of feed rods, growing crystal, and the melt is the same and the single crystals can be grown in FZ methods. But for incongruently melting materials a solvent (flux) disk is used at the trip of the feed rod to

grow single crystals in TSFZ method.

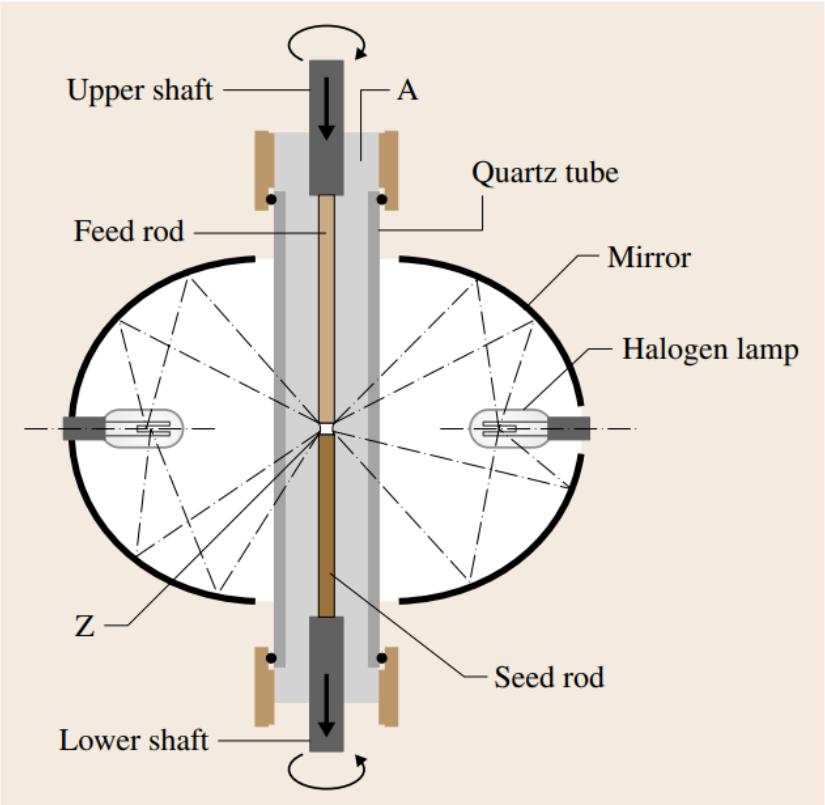

Fig. 2.1. Sematic diagram of FZ apparatus [7].

The composition of the solvent is different from feed rod and can be selected using the appropriate phase diagram. For example, solvent with a composition between C_1 and C_2 can precipitate an incongruently melting compound, C_0 shown in **Fig. 2.2**. In this method, molten solvent is supported against gravity mainly by the surface tension of the liquid which plays an important role to stable the molten zone in this method. Therefore, during the growth, a traveling solvent scheme must be maintained in which the feed is dissolved in the solvent and the relative proportions of the crystal are precipitated from the solvent. **Fig. 2.3** Schematic illustration of the traveling solvent floating zone method.

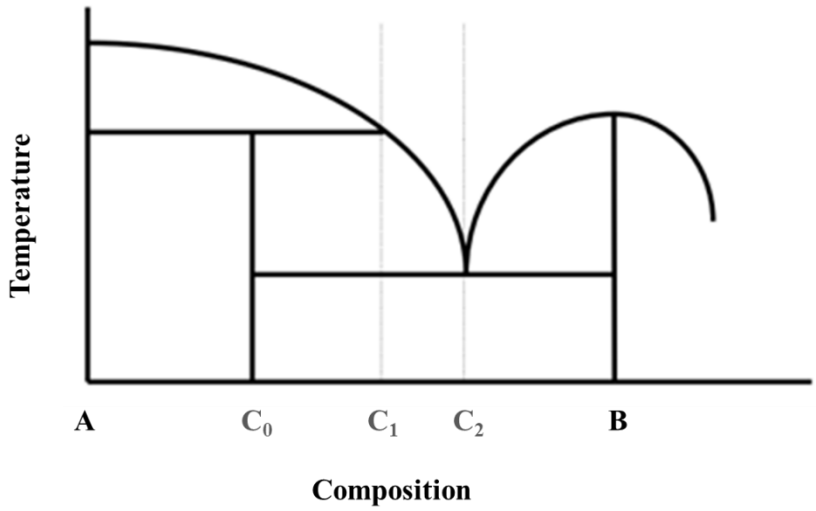

Fig. 2.2. Schematic diagram including an incongruently melting compound [8].

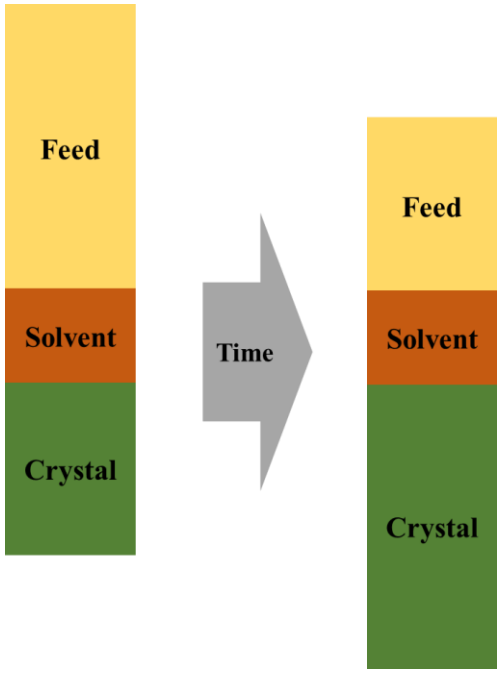

Fig. 2.3. Schematic illustration of the traveling solvent floating zone method.

The main advantages of the TSFZ are: single crystals can be grown from congruently and incongruently melting materials; crystals can be grown below their melting temperature. High purity large diameter crystals can also be grown in this method. In addition, in this method no container is used, hence there no interaction between the growing crystal and the container which reduces the contamination or defects of the grown crystals. Therefore, this method can be used for highly reactive materials, intermetallic compounds, oxides and refractory materials [8-14].

2.1.2. Convectional FZ Furnace and Tilting-mirror FZ Furnace

The conventional FZ furnace as shown in **Fig. 2.4** is widely used for the study of both single crystal growth and phase diagram. This furnace needs no crucibles, hence, there is no chance of chemical reaction between the melt and the crucible material. Also, this type of furnace can be used in traveling solvent scheme for growing incongruently melting materials and solid solution with uniform compositions. The rotation of feed rod and seed crystal can be controlled properly. The crystal growth rate can be optimized by controlling the upper and lower shaft movement. The gas (Ar or O_2 or N_2 or Air) flows within the growth chamber to create a suitable growth atmosphere. In this furnace, usually four heating lamps are used with four ellipsoidal mirrors. The ellipsoidal mirrors are used to focus the light on the feed rod to produce a molten zone. In conventional FZ furnace, the layout of the mirror and heating lamps are fixed in the same horizontal plane. On the other hand, the tilting-mirror-type FZ furnace, the mirror and heating lamps are tilted from 0° to 20º by a motor drive control [15]. Hence crystals can be grown at different tilting angles compared with conventional FZ furnace. **Fig. 2.5** shows the tilting-mirror-type FZ furnace with 0° and 10º mirror-tilting angles respectively.

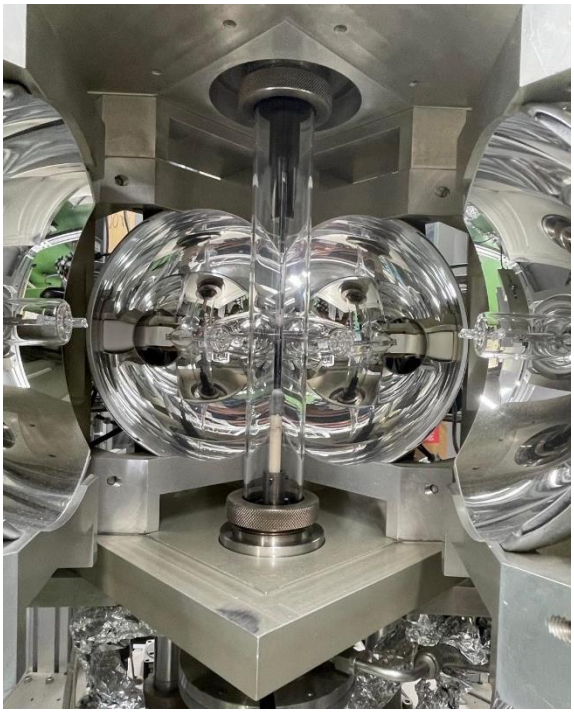

Fig. 2.4. Conventional FZ Furnace (Crystal Systems Inc., model: FZ-T-4000-H) at CCST, University of Yamanashi.

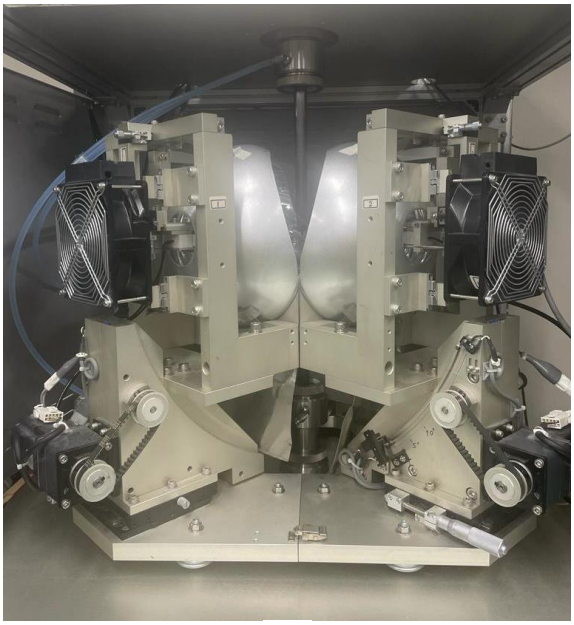

(a)

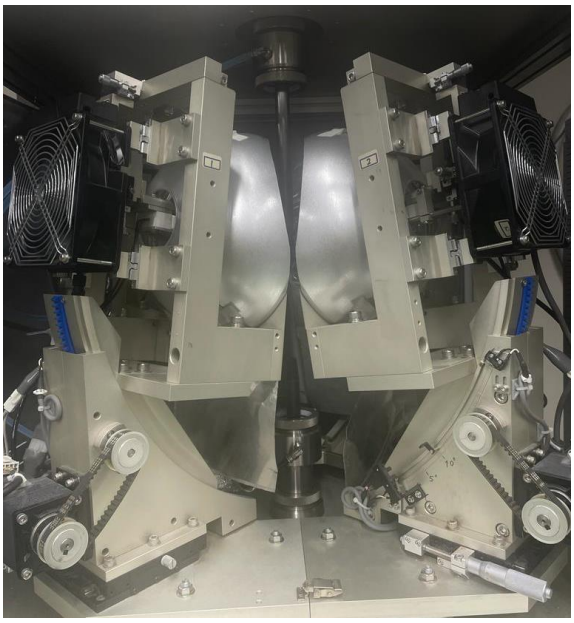

(b)

Fig. 2.5. Tilting-mirror FZ Furnace (Crystal System Inc., model: TLFZ-4000-H-VPO) with (a) 0° and (b) 10° mirror-tilting angles at CCST, University of Yamanashi.

2.2. Characterization techniques of grown crystals

2.2.1. X-ray Diffraction

X-ray diffraction analysis (XRD) is a technique used in materials science to determine the nature of the crystalline material. Crystals contain atoms, while X-rays can be considered as waves of electromagnetic radiation. The X-rays are directed towards the sample. When the circumstances are in accordance with Bragg's Law ($n\lambda = 2d\sin\theta$), the interaction of the incident rays with the sample results in constructive interference (and a diffracted ray). Then, these diffracted X-rays are identified, processed and counted. All the possible diffraction directions of the lattice are attained by adjusting the geometry of the incident rays, the orientation of the centered crystal and the detector. Conversion of the diffraction peaks to d-spacings allows identification of the sample. This is often accomplished by comparing the d-spacings with accepted reference patterns (such as JCPDS and ICDD database).

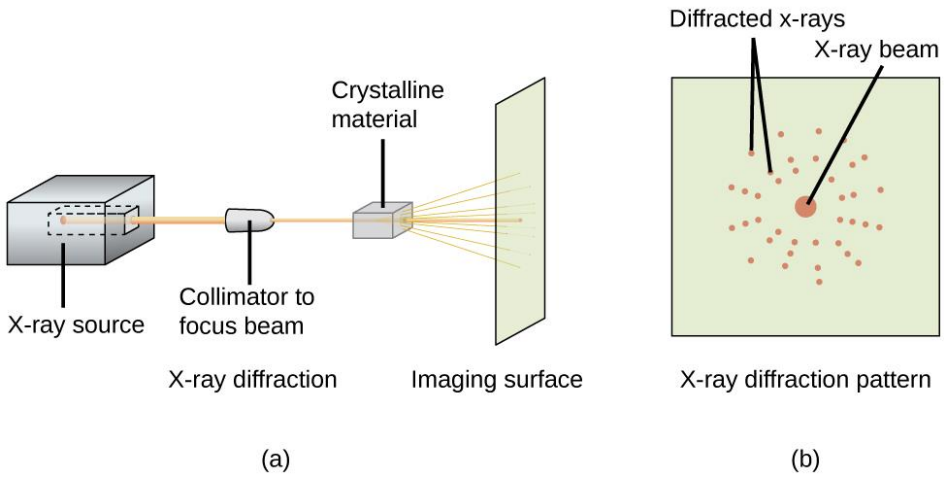

Fig. 2.6. Schematic diagram of Laue XRD method [16].

(a)

(b)

Fig. 2.7. (a) Two-dimensional and (b) Laue X-ray diffractometers at CCST, University of Yamanashi.

Also, the Laue method of XRD is mostly employed to identify the crystallographic orientation of single crystalline materials. Monochromatic radiation is replaced by white Bremsstrahlung in Laue diffraction. The images captured by this method appear as a series of scattered spots called Laue pattern. This Laue pattern indicates the crystallographic orientation of the sample by using the QLaue.exe software. **Fig. 2.6** shows the schematic diagram of Laue XRD method. **Fig. 2.7**. shows the images of X-ray diffractometers at our laboratory.

2.2.2. Atomic Absorption Spectrometer

Atomic absorption spectroscopy (AAS) is a spectroanalytical technique used to determine the concentration of metal atoms/ions in a sample. AAS detects elements in either liquid or solid samples. The atoms of the samples absorbed the light. After being subjected to light, generally from a hollow-cathode lamp, the free atoms of the sample undergo electronic transitions from the ground state to excited electronic states. The amount of light absorbed by the atoms is directly proportional to the concentration of the element in the sample. To lessen background interference, a monochromator is positioned in between the sample and the detector. The detector measures the intensity of the transmitted light and converts it to absorption data.

2.2.3. Scanning Electron Microscope

Scanning electron microscope (also known as SEM) is one of the most widely used instrumental methods for imaging the microstructure and morphology of the materials. Typically, a field emission gun or tungsten filament lamps is used as a source for the electron production. The ultrahigh vacuum conditions (10210 to 10211 Torr) are needed

for the field emission gun to keep the tip of the sample free from contaminants and oxide. The electron beam is accelerated through the high voltage system and then becomes narrowed after passing through electromagnetic lenses and apertures. The beam then uses scan coils to scan the specimen's surface. As the beam approaches and penetrates the material, several interactions take place that cause photons and electrons to be emitted from the sample surface. Images are generated after generating SEM type signals from the beam and sample interaction area. Various modes of SEM exist for material characterization including X-ray mapping, secondary electron imaging, backscattered electron imaging, electron channeling, and Auger electron microscopy. To get better surface topography analysis of a sample with the best spatial resolution, it needed to focus the required area at higher magnification levels (>100 k×) [17-18].

2.8. Image of Scanning Electron Microscope at CCST, University of Yamanashi.

2.2.4. Energy dispersive X-ray spectroscopy

Energy-dispersive X-ray spectroscopy (also known as EDS, EDX or XEDS) is one of the analytical techniques that enables chemical characterization and elemental analysis of a desired sample. It is commonly used with SEM. It depends on the interaction of some source of electromagnetic radiation (X-rays) excitation and the sample. The main working theory behind EDS is that 'core' electrons from an atom can be ejected by high energy X-rays. This theory, also referred to as Moseley's Law, established a direct connection between the atomic number of an object and the frequency of light it emits. A higher energy electron can fill the hole left by the removal of these electrons, and when it relaxes, it will release energy. By exposing a sample to X-rays, one may determine which elements are present and in what proportion by measuring the energy released during this relaxation process.

2.2.5. Electron Probe Micro Analyzer

The Electron Probe Microanalyzer (also known as EPMA) is an analytical instrument used for non-destructive elemental analysis of micro-sized volumes on the surface of the materials. The working principle of EMPA and SEM are equivalent. An electron beam is generally generated and directed to the specimen. When an electron beam is irradiated on a sample, inelastic collisions between the incident electron and electrons in the inner shells of atoms result in the production of distinctive X-rays. An inner-shell electron is ejected from its orbit and then a vacancy created. A higher-shell electron falls into this vacancy and must give up some energy as an X-ray. These quantized X-rays are allocated for compositional analysis of sample. Wavelength dispersive X-ray spectroscopy (WDS) separate the characteristic X-ray according on its wavelength and

2.9. Image of Scanning EPMA at University of Yamanashi.

accurately count the amount of X-ray at the specific range of the selected wavelength. Based on the comparison of captured characteristic X-ray of the sample and the standards, an algorithm has been developed to determine the chemical composition of the sample. When compared to EDS, WDS offers significantly greater energy resolution and signal-to-noise ratio.

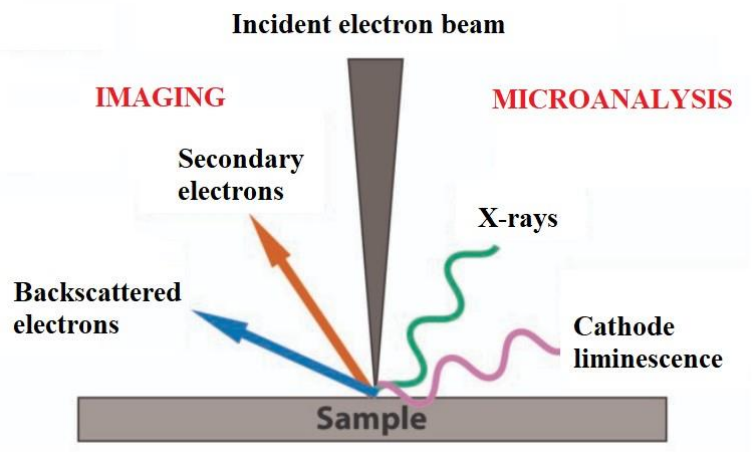

Fig. 2.10. Types of interactions of incident electron beam in SEM or EPMA [19].

2.2.6. Ionic conductivity and Activation energy

Electrochemical impedance spectroscopy (EIS) is commonly used to determine the ionic conductivity of solid electrolytes by analyzing the Nyquist plot. The equation for calculation of ionic conductivity is as follows:

$$\sigma = \frac{l}{ZA}$$

Where Z is the total impedance, l is the thickness and A is the area of the electrolyte sample. Typically, the impedance is dependent on the sinusoidal voltage frequency. When frequency is zero (i.e.; direct current (DC)), there is no difference between the impedance and resistance. Besides, the impedance arises in the alternating current (AC) circuit. Therefore, impedance is complex number and can be presented in Polar coordinates system as:

$$\hat{Z} = Ze^{i\theta}$$

here Z is the magnitude of impedance, θ is the phase difference (**Fig. 2.11**) and i is the

imaginary unit. In Cartesian coordinates system the complex impedance can be written as:

$$\hat{Z} = R + iX$$

Here, R and X is the real imaginary component of the complex impedance.

The activation energy (E_a) of conductivity can be calculated from the Arrhenius equation:

$$\sigma(T) = A \exp(-\frac{E_a}{kT})$$

where, E_a is the activation energy, σ is the ionic conductivity at temperature T, k is the Boltzmann constant and A is a pre-exponential factor [20-23].

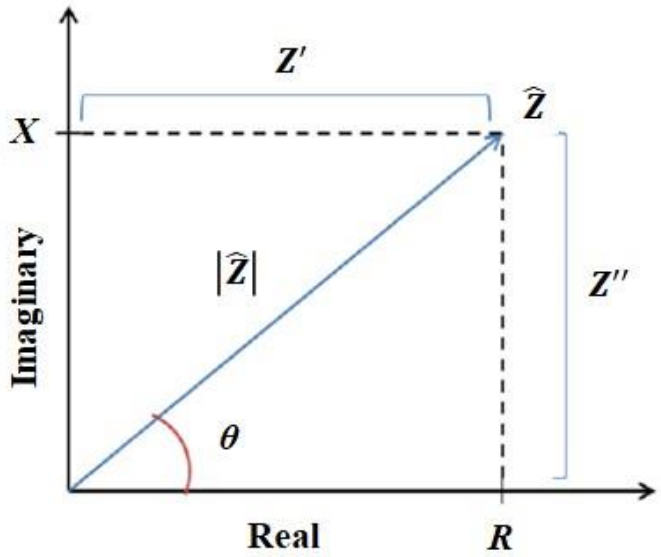

Fig. 2.11. Complex impedance graphed with respect to imaginary and real components [23].

2.2.7. Charging and discharging properties

A cell is generally composed of two active materials; negative electrode (also called anode), positive electrode (also called cathode), an electrolyte and current collector. The active materials may be metals, semiconductors, graphite or conductive polymers.

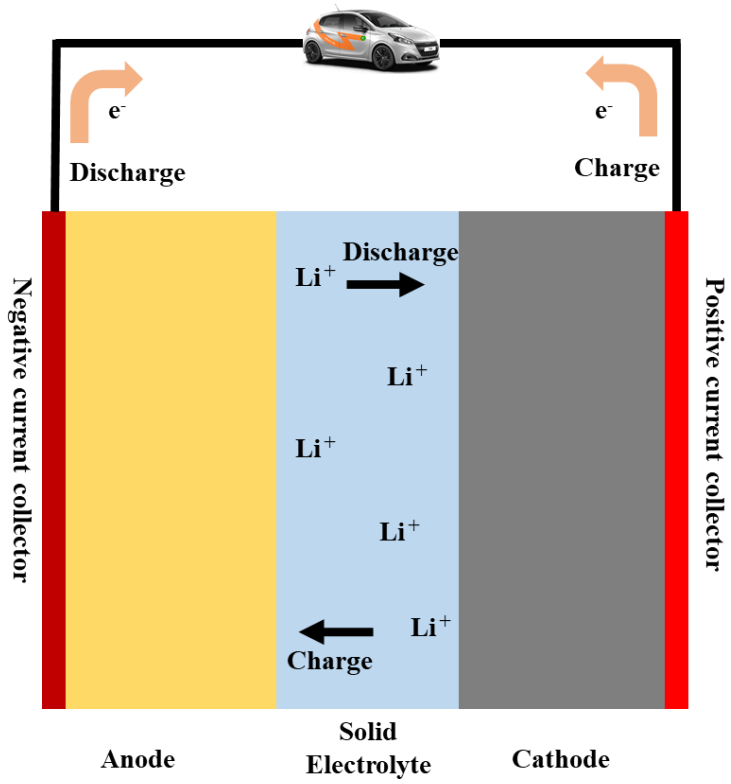

Fig. 2.12. Charge discharge process in solid-state LIBs.

On the other hand, organic liquid or inorganic solid or polymer can be used as electrolyte. When liquid electrolyte is used, a separator is needed to separate the electrodes for prevention of short circuit. The commonly used current collectors for the negative electrode (anode) and positive electrode (cathode) are copper and aluminum respectively. The active materials participate in the oxidation and reduction reactions. The positive electrode (cathode) is reduced and the negative electrode (anode) is oxidized during

discharging process. In this process, Li-ions are intercalated into the positive electrode (cathode) and de-intercalated from the negative electrode (anode). Besides, positive electrode (cathode) is oxidized and the negative electrode (anode) is reduced during charging process. In this process, Li-ions are de-intercalated into the positive electrode (cathode) and intercalated from the negative electrode (anode). The Li-ions movement is driven by the potential difference between the electrodes during charging discharging process. Then electrons flow through an external circuit to generate the current. **Fig. 2.12** shows the charging-discharging properties of solid-state Li-ion battery.

References

1) D. T. J. Hurle, *Hand Book of Crystal Growth* **2-A** 239 (1994).
2) J. J. Gilman, *The arts and Science of Growing Crystals, 2nd Edition* 347 (1996).
3) B. P. Bewlay, M. R. Jackson and P. R. Subramanian, *J. Opt. Mater.* **12** 32 (1999).
4) T. Duffar, *Crystal Growth Process Based on Capillarity, 1st Edition* 207 (2010).
5) R. Fornari, *Bulk Crystal Growth of Semiconductors: An Overview, Comprehensive Semiconductor Science and Technology* **3** 1 (2011).
6) G. Müller, and J. Friedrich, *Crystal Growth, Bulk: Methods. Encyclopedia of Condensed Matter Physics* 262 (2005).
7) H. A. Dabkowska and A. B. Dabkowski, *Crystal Growth of Oxides by Optical Floating Zone Technique. Springer Handbook of Crystal Growth* 367 (2010).
8) https://www.crystalsys.co.jp/pdf/fzmethod.pdf.
9) G. A. Wolff and A.I. Mlavsky, *Crystal Growth, Theory and Techniques, Ed. C.H.L. Goodman* 193 (1974).
10) W. G. Pfann, *Zone Melting, 2nd Edition* (1978).
11) Q. S. Chen and W. R. Hu, *Int. J. Heat. Mass. Transfer* **40 (4)** 757 (1997).
12) K. Byrappa, T. Ohachi, *Crystal Growth Technology, 3rd Edition* 565 (2003).
13) S. M. Koohpayeh, D. Fort, J. S. Abell, *Prog. Cryst. Growth Charact. Mater.* **54** 121 (2008).
14) R. Triboulet, *Handbook of Crystal Growth, Second edition, Part A, Chapter* **12** 459 (2015).
15) S. Nakamura, A. Maljuk, Y. Maruyama, M. Nagao, S. Watauchi, T. Hayashi, Y. Anzai, Y. Farukawa, C.D. Ling, G. Deng, M. Avdeev, B. Buchner and I. Tanaka, *Cryst. Growth Des.***19** 415 (2019).

16) https://chem.libretexts.org/@api/deki/files/61056/CNX_Chem_10_07_XRyDiff2.jpg?revision=1.

17) M. Omidi, A. Fatehinya, M. Farahani,Z. Akbari, S. Shahmoradi, F. Yazdian, M. Tahriri, K. Moharamzadeh, L. Tayebi and D. Vashaee, *Biomaterials for Oral and Dental Tissue Engineering* 97 (2017).

18) N. Raval, R. Maheshwari, D. Kalyane, S. R. Y. Ortiz, M. B. Chougule and R. K. Tekade, *Basic Fundamentals of Drug Delivery: Advances in Pharmaceutical Product Development and Research* 369 (2019).

19) https://emil.sites.unlv.edu/the-applications-of-epma-and-sem/

20) P. Vadhva, J. Hu, M. J. Johnson, R. Stocker, M. Braglia, D. J. L. Brett and A. J. E. Rettie, *Chem. Electro. Chem.* **8** 1930 (2021).

21) J. Gao, C. Wang, D.-W. Han and D.-M. Shin; *Chem. Sci.* **12** (2021) 13248 (2021).

22) M.-J. Uddin and S.-J. Cho, *Sustainable Energy Fuels* **2** 1458 (2018).

23) https://eng.libretexts.org/Bookshelves/Materials_Science/Supplemental_Modules_(Materials_Science)/Insulators/Electrochemical_Impedance_Spectroscopy.

Chapter 3

Traveling solvent floating zone growth and characterization of $Li_xLa_{(1-x)/3}TaO_3$ single crystals

3.1. Introduction

Double-perovskite-type oxides, which have layered structures and high ionic conductivity, are desirable solid electrolyte candidates for producing all-solid-state lithium-ion batteries (LIBs). $Li_{3x}La_{2/3-x}TiO_3$ (LLTiO) with double-perovskite structures, have high ionic conductivities (10^{-3} S·cm^{-1} at room temperature) [1-8]. However, Ti^{4+} can be easily reduced by Li-metal anodes, producing Ti^{3+} in higher-capacity LIBs [9-15]. In contrast, Ta^{5+} is resistant to reduction by Li-metal anodes. Therefore, $Li_xLa_{(1-x)/3}TaO_3$ (LLTaO) with a double-perovskite structure is a desirable solid electrolyte candidate for investigating high-capacity LIBs [12]. Mizumoto *et al*. [16-17] synthesized $Li_xLa_{(1-x)/3}TaO_3$ solid solutions *via* a solid-state reaction and measured the ionic conductivities with different Li compositions (x = 0–0.5). It was reported that the polycrystalline LLTaO exhibited a maximum ionic conductivity of 7×10^{-5} S·cm^{-1} with x = 0.18 (**Fig. 3.1**)

Because LLTaO (x = 0.18) has a tetragonal double-perovskite-type structure with lattice parameters (a = 3.94 Å and c = 7.96 Å at room temperature) [18], the conductivity of LLTaO is expected to be anisotropic. LLTaO single crystals are required for elucidating the anisotropic ionic conductivity and bulk properties with no grain boundaries.

In this study, single crystals of LLTaO were grown using the floating zone (FZ) and traveling solvent floating zone (TSFZ) methods. The TSFZ method, which uses solvents, is an extensive crystal-growth technique for incongruent-melting compounds such as LLTiO and LLNbO [19-20]. In addition, as the growth temperature can be lowered by the

solvent, the TSFZ method is expected to reduce the evaporation of the Li component from the melt. The growth conditions, such as the composition and the amount of solvent were optimized for the TSFZ growth. The composition and anisotropic ionic conductivity of LLTaO grown crystals were also investigated.

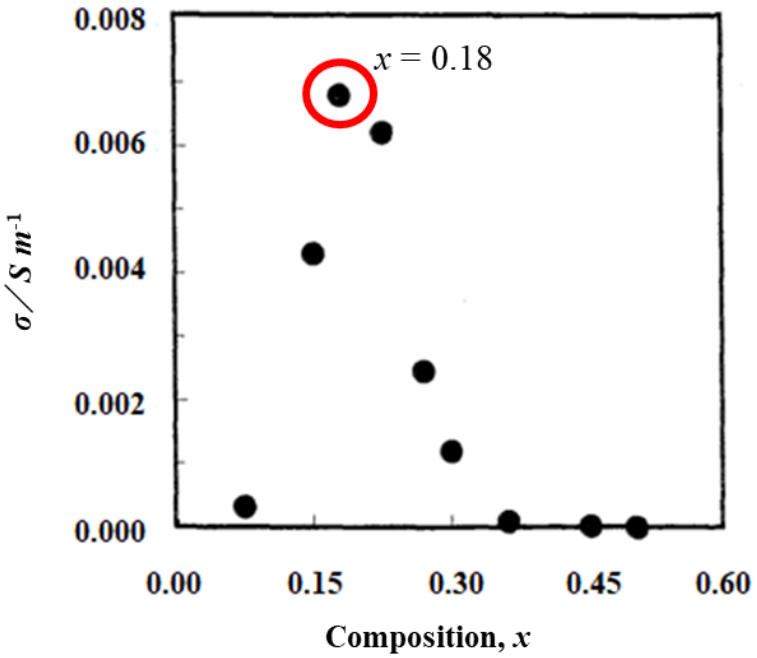

Fig. 3.1. Lithium ion conductivity of $Li_xLa_{(1-x)/3}TaO_3$ (x = 0.07-0.5) [16].

3.2. Experimental Procedure

Li_2CO_3, La_2O_3, and Ta_2O_5 (Rare Metallic Co., Ltd., 99.9% purity) were used as starting materials, weighed at an LLTaO (x = 0.18) stoichiometric composition, and mixed with ethanol. The mixed powder was dried and pre-calcined in the air at 800 °C for 2 h. The resulting powder was grounded and calcined in air at 1500 °C for 24 h. The calcined powder was grounded again and used for the feed rod preparation. Feed rods—approximately 6 mm in diameter and 50 mm in length—were prepared using the rubber

pressing method under a hydrostatic pressure of 300 MPa, and then sintered in the air at 1500 °C for 5 h. A solvent of 8% $LiTa_3O_8$-poor composition from LLTaO (x = 0.18) stoichiometric composition was used for the TSFZ growth. This solvent was prepared using the same procedure as the feed rod preparation. Subsequently, ~0.5 g of this solvent was added to the top of the feed rod. The crystal growth was performed in an optical FZ machine (Crystal Systems Inc., model FZ-T-4000-H) with four 1 kW halogen lamps. The growth rate was 5–10 mm/h. The growth atmosphere was Ar or O_2 (1 L/min). Feed and seed rotation rates were 10/20 rpm in opposite directions.

The orientation of the seed and grown crystals was confirmed by back-reflection Laue XRD (Rigaku Corp.) and two-dimensional XRD (Bruker Corp., model Discover D8 with a 2D detector). The inclusions and composition of the grown crystals were identified using scanning electron microscopy (SEM; Hitachi High-Tech, model TM-3030), energy-dispersive X-ray spectroscopy (EDS; Bruker Corp., model Quantax70), and electron probe microanalyzer (EPMA; JEOL Ltd., model JXA-iHP200F). The crystals were cut and polished to a mirror surface, and subsequently coated with carbon for SEM and EPMA analysis. The concentrations of Ta and La in the grown crystals were analyzed by EPMA quantitative analysis using the single crystals of $BaTa_2O_6$ and $La_2Ti_2O_7$ as standard samples respectively. The Li concentration x in the LLTaO crystals was determined from the $Li_xLa_{(1-x)/3}TaO_3$ formula using the analytical values of Ta and La. In addition, the Li concentration in the grown crystal was directly analyzed using an atomic absorption spectrometer (AAS; Hitachi High-Tech Science, model Z-2300). The sample dissolution method for AAS analysis is as follows; “Samples of grown crystals were ground to a fine powder. The ground sample was hydrolyzed with nitric acid and hydrofluoric acid, dissolved in dilute nitric acid, and filtered. Insoluble materials were decomposed by

heating with sulfuric acid and nitric acid, and then dissolved with dilute nitric acid." The Li^+ ion conductivity of the grown crystals was measured using the AC complex-impedance method. To clarify the anisotropy of the ionic conductivity, the crystal orientation of the grown crystals was adjusted to be parallel and perpendicular to the *c*-axis. The grown crystals were cut to a thickness of approximately 0.8 mm. The sliced samples were polished and sputtered with Au-Pd on both sides to maintain the ohmic contact of the electrode. The complex impedance of the samples was measured in the frequency range of 1 kHz~10 MHz at a temperature range of 25–225 °C using an inductance-capacitance-resistance meter (Iwatsu Electric Co., Ltd., model PSM 1735).

3.3. Results and Discussion

3.3.1. Crystal growth by the floating zone method

First, we attempted to grow single crystals of LLTaO with $x = 0.18$ using the conventional FZ method. The as-grown crystal of LLTaO and the SEM image of the cross-section parallel to the growth direction in the crystal are shown in **Fig. 3.2.** It was difficult to maintain the molten zone owing to the contact problem between the feed rod and the grown crystal during the crystal-growth process. Consequently, the Ta-rich phase was deposited as inclusions in the grown crystal, as shown in the SEM and EPMA results. This result not only indicates that LLTaO melts incongruently with the Ta-rich phase and liquid but also suggests the LLTaO phase was deposited from a melt with a lower Ta concentration than the LLTaO stoichiometric composition. Unfortunately, the composition of the inclusions and the Ta-rich phases could not be determined by SEM or EPMA due to the undetectable Li^+ ion. However, the La_2O_3-Li_2O-Ta_2O_5 system phase

diagram suggests that the Ta-rich phase could be $LiTa_3O_8$, $La_2Ta_{12}O_{33}$, $LaTa_3O_9$, or Ta_2O_5, rather than LLTaO ($x = 0.18$).

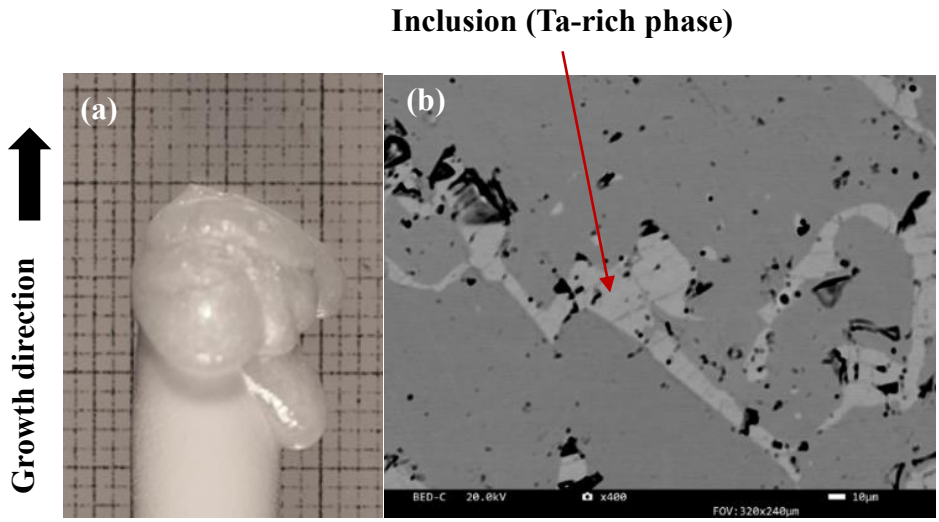

Fig. 3.2. (a) LLTaO crystal grown using the FZ method. (b) SEM image of the cross-section parallel to the growth direction in the LLTaO crystal.

3.3.2. Crystal growth by the travelling solvent floating zone method

The Ta-rich phase was regarded as $LiTa_3O_8$, and LLTaO single crystals were grown *via* the TSFZ growth process using a solvent with 8% $LiTa_3O_8$-poor composition from the LLTaO feed composition. The amount of solvent is very important for maintaining the molten zone during the TSFZ growth process. In this work, approximately 0.5 g of the solvent amount for a 6 mm feed diameter was optimum for supporting the TSFZ growth. When more than 0.5 g of solvent was utilized, the molten zone was too long and became unstable for a long time. As shown in **Fig. 3.3**, the crystals were grown in O_2 and Ar atmospheres to optimize the growth atmosphere. For crystal growth in O_2 atmosphere, a high lamp power was required to melt the feed rod due to the reflection of white color feed rod, and the enhanced evaporation of the lithium component from the molten zone

made the quartz tube surrounding the growth area smoky. Because of the unstable molten zone in the O_2 atmosphere, many cracks were found in the grown crystals.

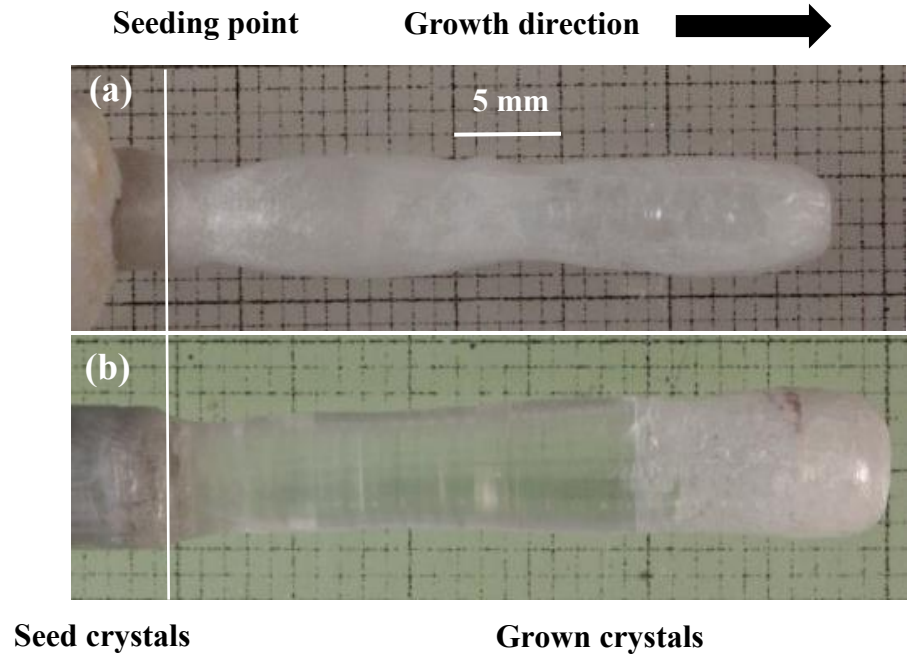

Fig. 3.3. LLTaO crystals grown in (a) O_2 and (b) Ar atmosphere using the TSFZ method.

In addition, some cleavages parallel to the (001) plane were observed in the grown crystals. However, in the Ar atmosphere, the crystals were grown at a lower lamp power than that in the O_2 atmosphere. This is because the feed rods were colored by the reduction of the Ta ions from pentavalent to tetravalent in the LLTaO feed at a high temperature. As a result, comparatively low lithium evaporation occurred, and the molten zone was stable for a long time during the TSFZ growth process. The optimum growth rate was determined to be 5 mm/h to maintain a stable molten zone for a long time, whereas contact between the crystal and feed occurred at a growth rate higher than 5 mm/h. When LLTaO crystals were grown at a rate of 5 mm/h in the Ar atmosphere (1 L/min), the as-grown

crystals were crack-free and exhibited black color owing to an oxygen-deficient environment. The grown crystals turned colorless and transparent when left overnight in the air at room temperature.

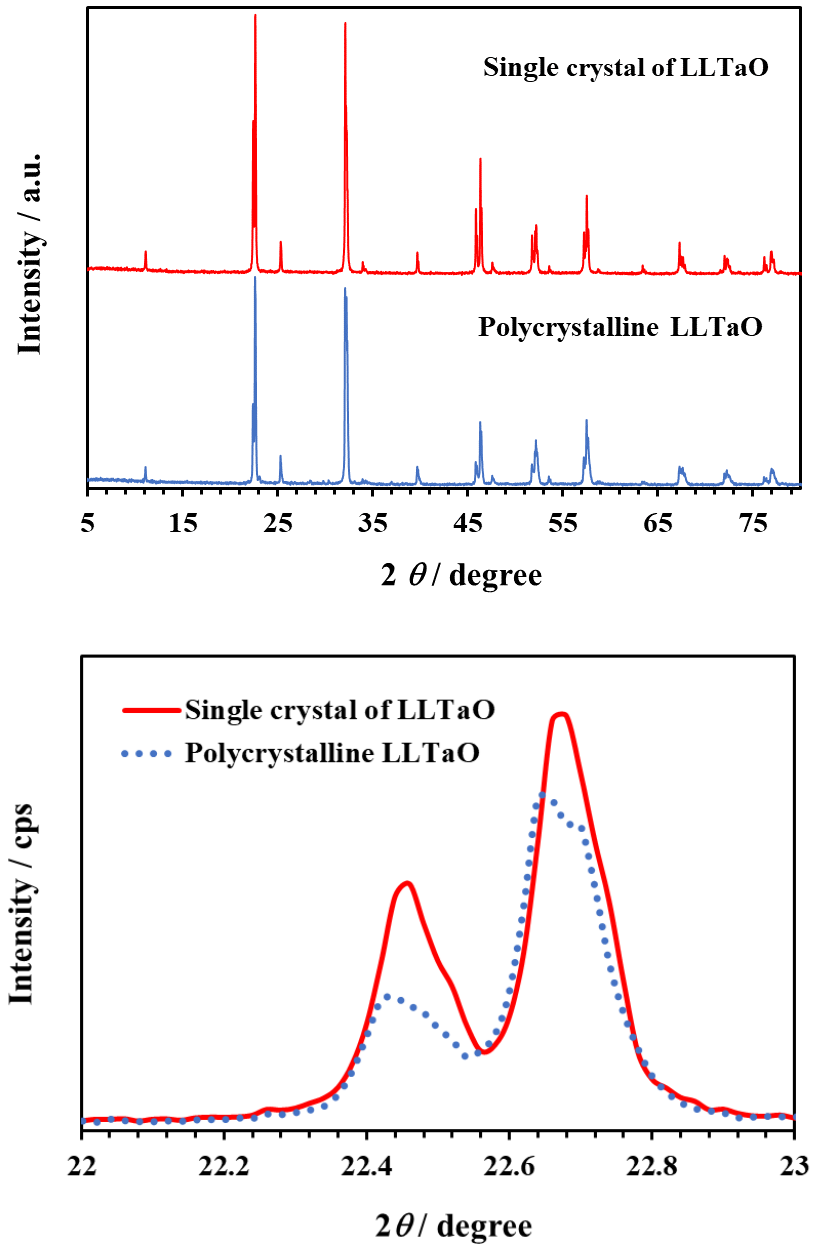

Fig. 3.4. Powder XRD-pattern of LLTaO.

3.3.3. Characterization of grown crystals

To clarify the crystallinity of single crystal and polycrystal we have added the powder XRD-pattern of LLTaO. The X-ray diffraction peaks of LLTaO single crystal and its polycrystal are shown **Fig. 3.4**. LLTaO shows the double perovskite tetragonal crystal structure. The sharp and high intensity X-ray diffraction peaks show the high crystallinity of single crystal than that of polycrystal. Hence, polycrystal shows higher crystal defects than that of single crystal.

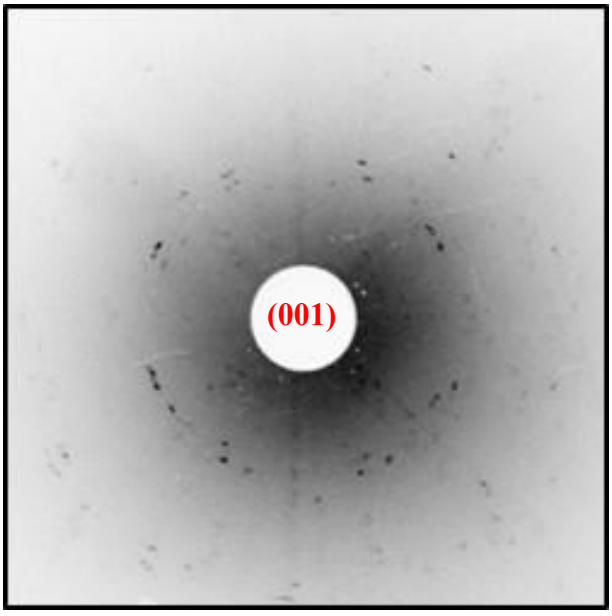

Fig. 3.5. Back-reflection Laue XRD image of (001) perpendicular to the growth direction of the LLTaO grown crystal.

The grown crystals were confirmed to be single crystals by back-reflection Laue XRD perpendicular to the growth direction (**Fig. 3.5**). The growth direction was determined to be [110] by back-reflection Laue XRD and two-dimensional XRD. The composition and

homogeneity of the grown LLTaO crystals were quantitatively analyzed using EPMA (**Fig. 3.6**). The distribution of the La/Ta atomic ratio in the LLTaO phase is almost homogeneous along the growth direction. The La/Ta atomic ratio in the LLTaO phase was determined to be 0.306 ± 0.008, and the Li concentration x was 0.08 ± 0.01, which was determined by the La/Ta atomic ratio and the $Li_xLa_{(1-x)/3}TaO_3$ composition formula.

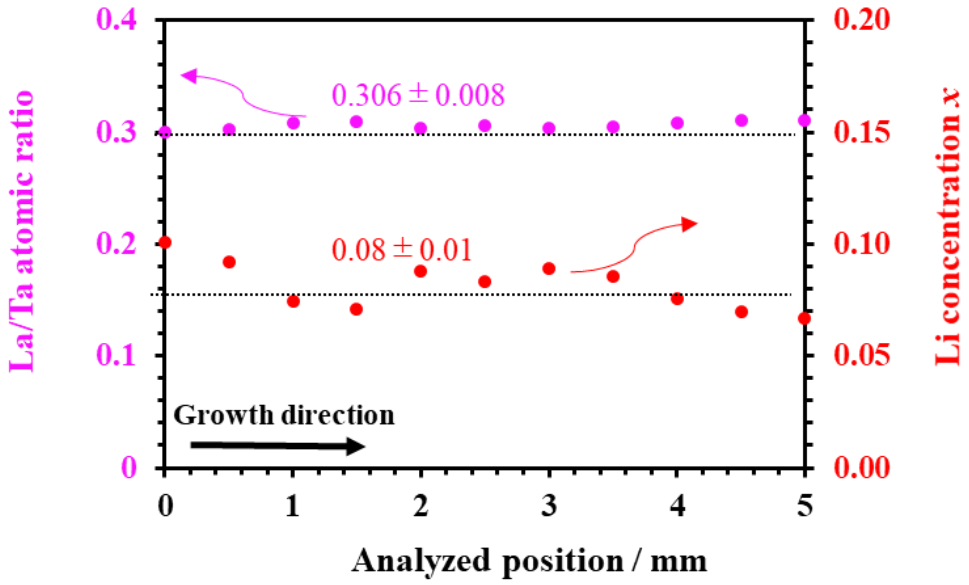

Fig. 3.6. La/Ta atomic ratio and distribution of Li concentration along the growth direction in the LLTaO grown crystal. The dotted lines show the average values respectively.

The Li concentration x, which was analyzed using AAS, was consistent with the measurement error, showing the value of x = 0.086 ± 0.001. The Li concentration in the grown crystals was remarkably lower than that of the nominal composition, in which x was 0.18 owing to the lower Li concentration in the solvent and Li evaporation during the

crystal-growth process. The Li and Ta concentrations in the solvent may be optimized to control the Li concentration in the LLTaO single crystals.

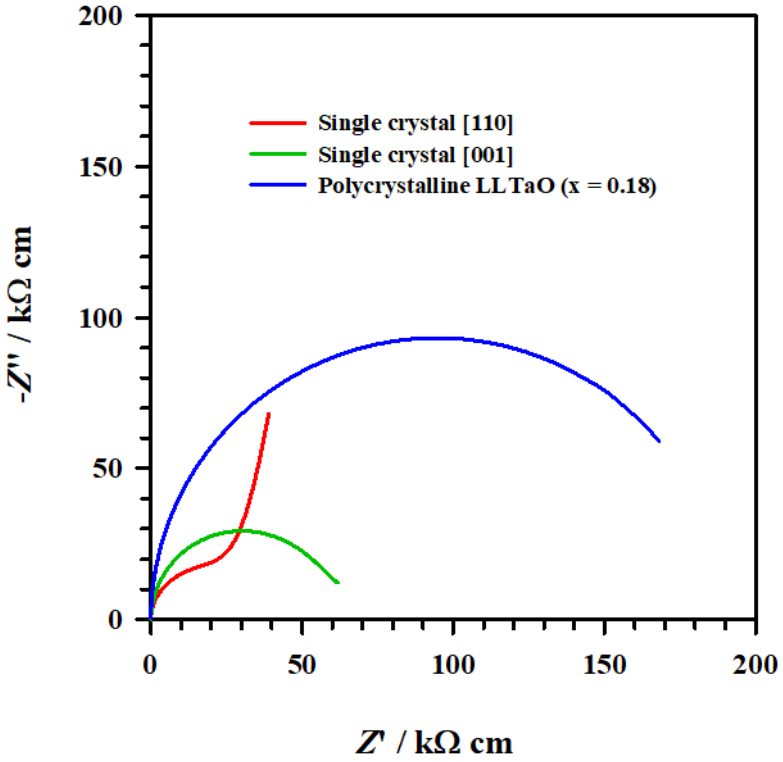

Fig. 3.7. Nyquist plots of LLTaO at room temperature.

The ionic conductivities along the [110] and [001] directions in the grown crystals of LLTaO were measured to clarify the anisotropy of the ionic conductivity. Nyquist plots of LLTaO at room temperature are shown in **Fig. 3.7.** The calculated ionic conductivities of LLTaO are listed in **Table 3.1**. The ionic conductivity along the [110] growth direction, $\sigma_{[110]}$ = 2.8 ×10^{-5} S·cm^{-1}, was higher than that along [001], $\sigma_{[001]}$ = 1.8 ×10^{-5} S·cm^{-1}, and the anisotropic parameter was 1.56. The ionic conductivities of double perovskite tetragonal single crystals of LLTiO [19]; $\sigma_{[110]}$ = 1.6 ×10^{-3} S·cm^{-1} and $\sigma_{[001]}$ = 5.26 × 10^{-4} S·cm^{-1} along [110] and [001] and for LLNbO [20]; $\sigma_{[100]}$ = 1.2 × 10^{-4} S·cm^{-1} and $\sigma_{[001]}$ =

7.4×10^{-5} S·cm^{-1} along [100] and [001] respectively at room temperature. Hence, Li^+ mobility perpendicular to the *c*-axis is higher than that parallel to the *c*-axis owing to the crystal structure of LLTiO, LLNbO and LLTaO. Although the Li concentration of 0.086 in the grown crystals is very low, the ionic conductivity of the single crystals is three times higher than that of polycrystalline LLTaO with $x = 0.18$ in **Table 3.1**, which is the maximum ionic conductivity ($\sigma = 7 \times 10^{-5}$ S·cm^{-1}) in the reported data of LLTaO [18].

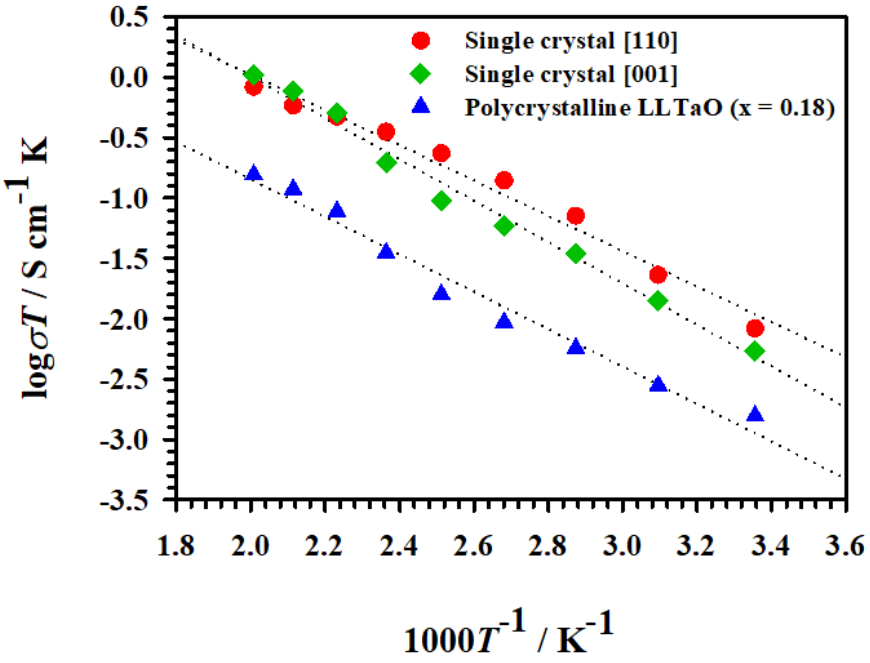

Fig. 3.8. Temperature dependence on ionic conductivity in LLTaO.

The temperature dependence of the ionic conductivity of the grown crystals in the range of room temperature to 498 K is shown in **Fig. 3.8**. The plots exhibit a nearly linear relationship, and the activation energy was determined from the slope of these plots (**Fig. 3.8, Table 3.1**). The calculated activation energies $E_{a[110]}$ and $E_{a[001]}$ were 0.29 and 0.34 eV, respectively. The activation energies of LLTaO ($x = 0.086$) grown crystals are much lower than that of the reported polycrystalline LLTaO ($E_a = 0.39$ eV for $x = 0.18$) [21].

This may be related to the crystallinity and the defect density between single crystals and polycrystals.

Table 3.1. Ionic conductivities at room temperature and activation energies of LLTaO samples.

Sample	Ionic conductivity σ (10^{-5} S·cm^{-1})	Activation energy E_a (eV)
Single crystal [110]	2.8	0.29
Single crystal [001]	1.8	0.34
Polycrystalline LLTaO (x = 0.18)	0.53	0.31

The activation energy E_a is an important parameter for controlling the Li^+ mobility in LLTaO. The double-perovskite tetragonal crystal structure causes the random distribution of La^{3+} in La-poor and La-rich layers, doubling the *c*-axis of the cell parameter, and tilting the TaO_6 octahedra. The double perovskite tetragonal structure of LLTaO is shown in **Fig. 3.9**. In the crystal structure of LLTaO, Li^+ and La^{3+} are occupied in La-rich layers, whereas La-poor layers are fully empty. Although Li^+ can migrate along the *ab*-plane and the *c*-axis, La-rich layer hinders the migration of Li^+. Thus, Li^+ ions could easily migrate from one La^{3+} vacancy to another along the *ab*-plane rather than the *c*-axis. However, the bottleneck size influences the Li^+ migration and activation energy. When the bottleneck size increases, it causes the decrease of activation energy i.e; increases of Li-ion conductivity. Therefore, the activation energy along the *ab*-plane is lower than that along the *c*-axis. Deviation of the ionic conductivity from the linear relationship at a high temperature was observed as shown in **Fig. 3.8**. The behavior was also reported only for La in $R_{0.25}Li_{0.25}TaO_3$ (R = La, Nd, Sm, and Y) [9] and for x = 0.075 ~ 0.30 in $La_{(1-}$

$_{x)/3}Li_xTaO_3$ [17]. Furthermore, Li-ion dynamics and activation energy in LLTaO may be different from those at a lower temperature.

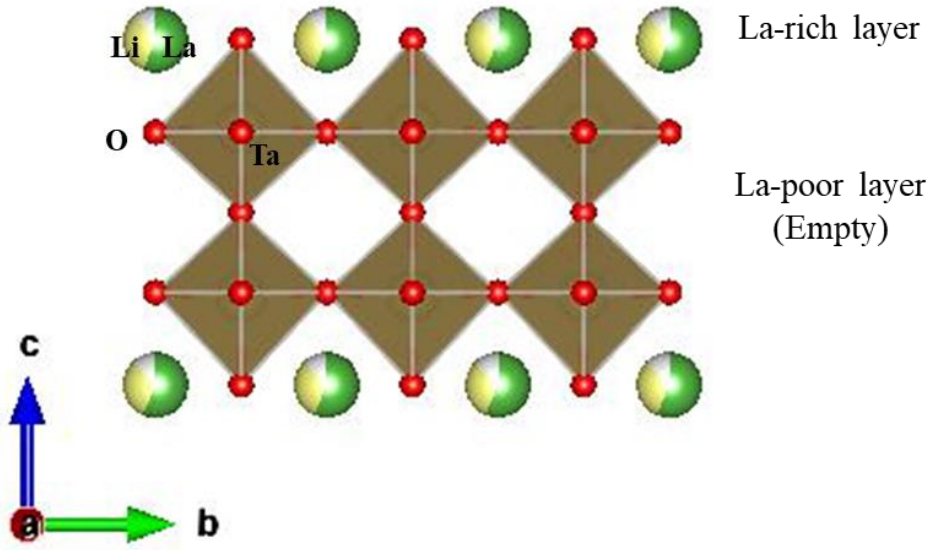

Fig. 3.9. Crystallographic structure of LLTaO.

3.3.4. Electrochemical properties of LLTaO single crystals

To characterize the electrochemical properties of LLTaO, we prepared the UFO cells using LLTaO single crystals as solid electrolyte. The planes of the crystals were identified using Laue XRD and two-dimensional XRD images. The crystals were cut perpendicular (001) and parallel (110) to the growth direction with thickness of about 300 ~ 350 μm. Then the both sides of the samples were polished smoothly very carefully. Because the samples were easily broken during polishing. Then the Au was sputtered on one side of the samples. The UFO cells were prepared using NCM 523 cathode material, sputtered LLTaO ((110) or (001)) as solid electrolyte and Li-metal as anode. The cells were prepared in vacuum chamber known as glove box. The EIS results and then charge-discharge properties of the cells were observed as shown in **Fig. 3.11**. No operation was observed

may due to the short circuit of the cells. To avoid this problem, we used a separator between electrodes and electrolyte and then cells were prepared for both samples (110) and (001). However, no operation was observed as shown in **Fig. 3.12**. It may due to the high internal resistance of the cells. Hence, by reduction of cell resistance, it may be observed the charge-discharge properties of LLTaO solid electrolyte base solid-state Li ion batteries.

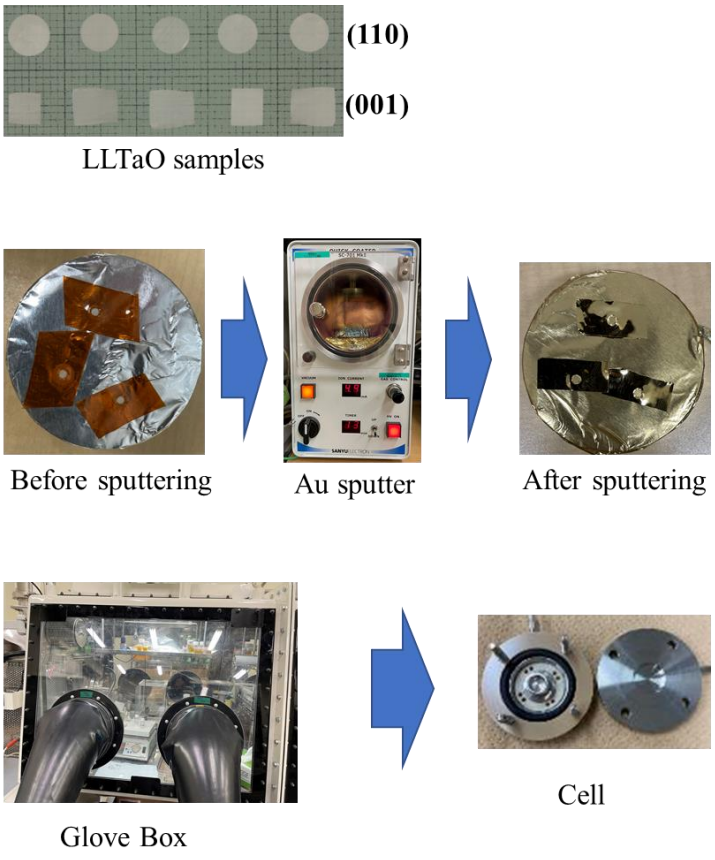

Fig. 3.10. Cell preparation for electrochemical properties of LLTaO single crystals.

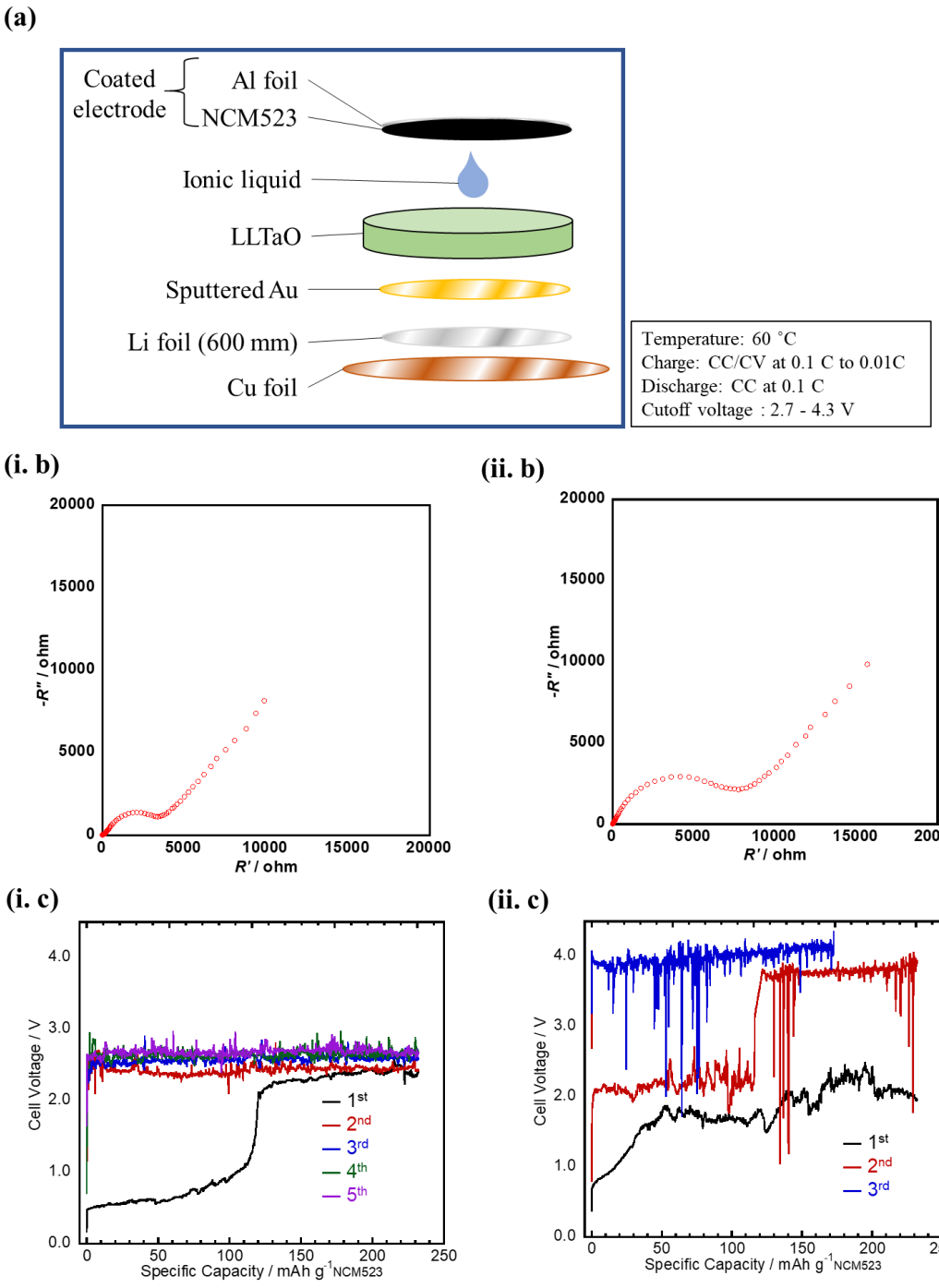

Fig. 3.11. (a) Schematic diagram of cell without separator, (b) EIS results and (c) charge-discharge results using (i) LLTaO (110) and (ii) LLTaO (001) samples respectively.

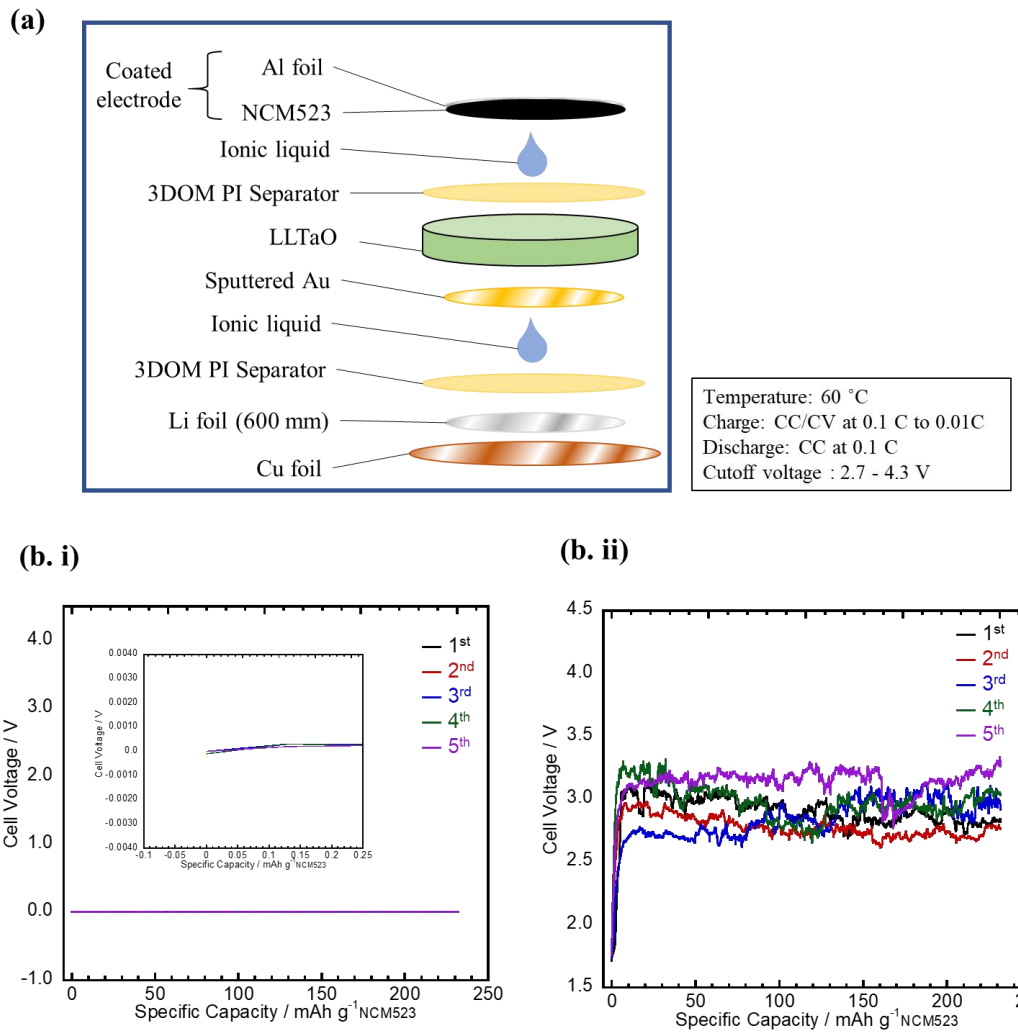

Fig. 3.12. (a) Schematic diagram of cell with separator and (b) charge-discharge results using (i) LLTaO (110) and (ii) LLTaO (001) samples respectively.

3.4. Conclusion

Inclusion- and crack-free transparent bulk single crystals of LLTaO were successfully grown using the TSFZ growth method in a Ta-poor solvent (8% $LiTa_3O_8$-poor composition from LLTaO) in the Ar atmosphere. The grown crystals exhibited black color due to oxygen deficiency in the growth atmosphere. When the crystals were left overnight in the air at room temperature, they became colorless and transparent. This phenomenon suggests that oxygen diffusion is rapid even at room temperature, which is very interesting not only in the aspect of lithium ion conduction but also in oxygen conduction. The LLTaO crystals grown using the feeds of $x = 0.18$ showed a uniform Li concentration of 0.086 ± 0.001, which was lower than that of the feed because of the Li-poor solvent and Li evaporation during crystal growth. The anisotropic ionic conductivities of the grown crystals were determined to be $\sigma_{[110]} = 2.8 \times 10^{-5}$ S·cm^{-1} and $\sigma_{[001]} = 1.8 \times 10^{-5}$ S·cm^{-1}. Therefore, the Li^+ mobility perpendicular to the *c*-axis is higher than that parallel to the *c*-axis, indicating that the LLTaO single crystals oriented parallel to the *c*-axis are desirable substrates for producing next-generation solid-state Li-ion batteries. To characterize the electrochemical properties of LLLTaO, we prepared the UFO cells using LLTaO single crystals as solid electrolyte. But, no operation was observed may due to the short circuit or internal high resistance of the cells.

References

1) Y. Inaguma, L.Q. Chen, M. Itoh, T. Nakamura, T. Uchida, H. Ikuta and M. Wakihara, *Solid State Commun.* **86** 689 (1993).

2) Y. Harada, H. Watanabe, J. Kuwano and Y. Saito, *J. Power Sources* **81-82**, 7771 (1999).

3) A. Rivera, C. Leon, J. Santamaria, A. Varez, M.A. Paris and J. Sanz, *J. Non-Cryst. Solids* **307-310** 992 (2002).

4) K. Yu, Y. Tian, R. Gu, L. Jin, R.P. Ma, H.C. Sun, Y.L. Xu, Z. Xu and X.Y. Wei, *J. Eur. Ceram. Soc.* **38** 4483 (2018).

5) R. Li, K. Liao, W. Zhou, X. Lia, D. Mengb, R. Cai and Z. Shao, *J. Membr. Sci*. **582** 194 (2019).

6) D. Lakshmi, B. Nalini, S. Jayapandi and P. Christopher Selvin, *J. Mater. Sci.: Mater. Electron.* **31** 1343 (2020).

7) D.-L. Lu, R.-R. Zhao, J.-L. Wu, J.-M. Ma, M.-L. Huang, Y.-B. Yao, T. Tao, B. Liang, J.-W. Zhai and S.-G. Lu, *J. Eur. Ceram. Soc.* **40** 2396 (2020).

8) M. S. Ali, Y. Maruyama, M. Nagao, S. Watauchi and I. Tanaka, *Solid State Ionics* **350** 115330 (2020).

9) K. Mizumoto and S. Hayashi, *Solid State Ionics* **116** 263 (1999).

10) C. Y. Sun and K. Z. Fung, *Solid State Commun.* **123** 431 (2002).

11) S. Stramare, V. Thangadurai and W. Weppner, *Chem. Mater.* **15** 3974 (2003).

12) M. Vijayakumar, J. Emery, O. Bohnke, R. L. Vold and G. L. Hoatson, *Solid State Ionics* **177** 1673 (2006).

13) P. Knauth, *Solid State Ionics* **180** 911 **(**2009).

14) K. K. Bharathi, H. Tan, S. Takeuchi, L. Meshi, H. Shen, J. Shin, I. Takeuchi and L. A. Bendersky, *RSC Adv.* **6** 61974 (2016).

15) R. Yu, Q. -X. Du, B .-K. Zou, Z. -Y. Wen and C. -H. Chen, *J. Power Sources* **306** 623 (2016).

16) K. Mizumoto and S. Hayashi, *J. Ceram. Soc. Jpn.* **105** 713 (1997).

17) K. Mizumoto and S. Hayashi, *J. Ceram. Soc. Jpn.* **106** 369 (1998).

18) W. Araki, Y. Nagakura and Y. Arai, *Ceram. Int.* **46** 6270 (2020).

19) Y. Maruyama, S. Minamimure, C. Kobayashi, M. Nagao, S. Watauchi and I. Tanaka, *R. Soc. Open Sci.* **5** 181445 (2018).

20) M. S. Ali, N. Sato, I. Fukasawa, Y. Maruyama, M. Nagao, S. Watauchi and I. Tanaka, *Cryst. Growth Des.* **19(11)** 6291 (2019).

21) K. Mizumoto and S. Hayashi, *Solid State Ionics* **127** 241251 (2000).

Chapter 4

Growth of Large-diameter $Li_xLa_{(1-x)/3}NbO_3$ Single Crystal by the TSFZ method using a tilting-mirror FZ furnace

4.1. Introduction

In the last decades, rechargeable lithium-ion batteries (LIBs) are widely used as continuous power sources for portable electronic devices, electric/hybrid electric vehicles, marine vehicles, autonomous aircraft, smart grids, solar power storage systems, robots etc. [1-9]. In most of the commercial LIBs, organic liquid electrolytes or polymer-based electrolytes are used but these possess dendrite formation, leakage, short circuit and flammability problems. Others some inorganic solid electrolytes such as sulfides, glasses or oxides may expected as electrolytes for the next generation LIBs. Glasses and sulfides have high ionic conductivity but these are air exposure and produce environmentally toxic hydrogen sulfide. In addition, solid sulfides may react with lithium metal and cause short circuit problem in LIBs [10-15]. Compared to other electrolytes, oxide solid electrolytes are environmentally safe in use but these possess typically low ionic conductivity. In addition, grain boundaries and random crystallographic orientation in polycrystalline oxide solid electrolyte decrease its ionic conductivity. So, research on single crystal of oxide solid electrolytes is very important for developing the all solid-state LIBs. Single crystal of solid electrolyte possesses unique properties due to their continuous, uniform and highly-ordered structure. However, single crystals have no void or grain boundary. For these, there is also no chance of dendrite formation from cathode to anode and thereby increase the lifetime and safety issues of LIBs [13, 16-17].

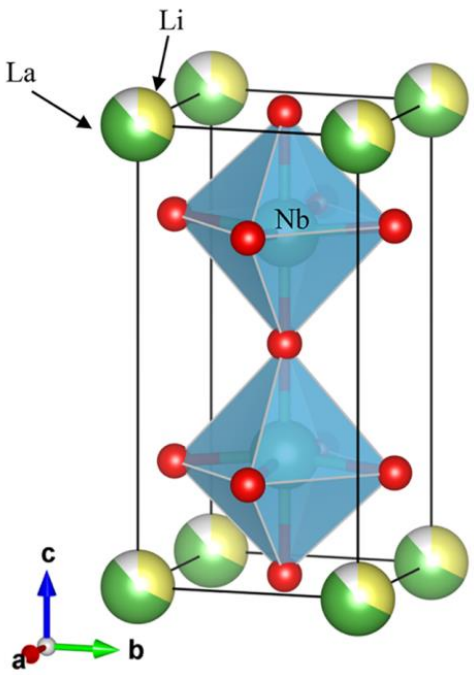

Fig 4.1. Crystallographic structure of $Li_xLa_{(1-x)/3}NbO_3$.

$Li_xLa_{(1-x)/3}NbO_3$ (here after called LLNbO) with high ionic conductivity (more than 10^{-4} $S{\cdot}cm^{-1}$) is a candidate of the oxide solid electrolytes for solid-state LIBs application [18-21]. LLNbO shows anisotropic ionic conductivity due to its double-perovskite crystal structure in which La^{3+} occupied layers and La^{3+} vacant layers stack alternatively along the *c*-axis as shown in **Fig 4.1**. The polycrystalline LLNbO with lithium concentration $x = 0.10$ shows the ionic conductivity of $\sigma = 4.7 \times 10^{-5}$ $S{\cdot}cm^{-1}$. However, it was difficult to find out the anisotropic ionic conductivity of polycrystalline LLNbO due to its grain boundaries. On the other hand, Y. Fujiwara e*t.al.*, investigated the anisotropic ionic conductivity of LLNbO single crystals grown by directional solidification method for the first time [19]. But the lithium concentration was not distributed homogenously in the grown crystal; furthermore, the lithium concentration increases continuously as crystal

growth proceeds. They investigated the ionic conductivity of LLNbO single crystals with various lithium concentration of x. They found that LLNbO single crystals with a lithium concentration of x = 0.08 shows the maximum ionic conductivity ($\sigma = 3.6\times10^{-4}$ S·cm^{-1}) as shown in **Fig. 4.2**. Recently, in our laboratory, the TSFZ method has been used to grow homogenous single crystals of LLNbO with a diameter of approximately 6 mm and length of 35 mm. The structural changes, lithium concentration-dependent ionic conductivity, activation energy, and lithium concentration distribution of LLNbO were reported. In addition, the investigation of the Li-ion conductivity of LLNbO single crystals with different Li concentrations (0.034 to 0.114) has been performed (**Fig. 4.3**). It was observed that, when Li concentrations x = 0.1 in LLNbO feeds within the range of $0.05 \leq x \leq 0.15$, the grown crystals with Li concentration $x \sim 0.07$ shows the highest ionic conductivity [20-21].

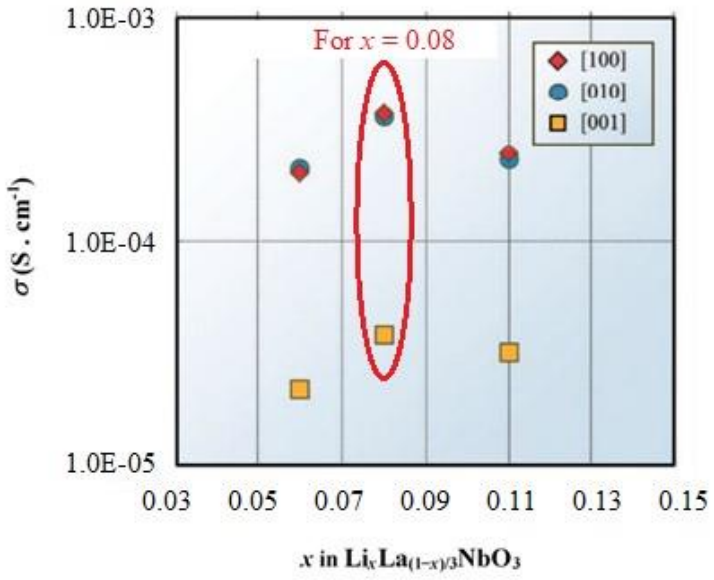

Fig. 4.2. Anisotropic ionic conductivity along the [100], [010] and [001] directions of $Li_xLa_{(1-x)/3}NbO_3$ single crystals [19]

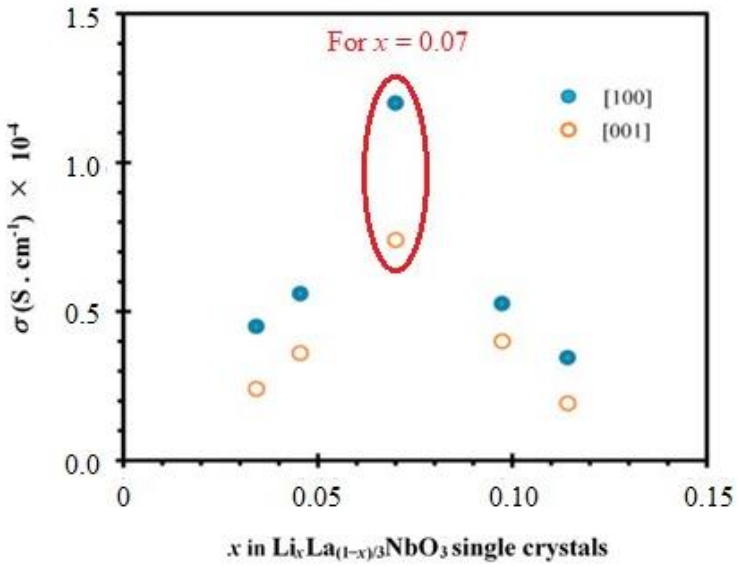

Fig. 4.3. Anisotropic ionic conductivity along the [100] and [001] directions of $Li_xLa_{(1-x)/3}NbO_3$ single crystals annealed in oxygen [21].

The phase diagram of LLNbO, solubility limit and distribution coefficient were investigated for the high-quality grown crystals. LLNbO shows incongruent melting behavior in $LaNbO_4$ and liquid formation [22]. Travelling solvent floating zone (TSFZ) is an extensive crystal growth technique for incongruent melting behavior compounds such as $Y_3Fe_5O_{12}$ and $La_{2-x}Si_xCuO_4$. In TSFZ grows we can grow comparatively large single crystals without contamination. However, crystals are grown below their melting temperature which reduces the Li evaporation, nonstoichiometric defects and dislocation densities during grows [23-26].

Devices and technological applications of all solid-state batteries require the large-diameter crystals. However, there are no reports of high-quality, inclusion-free large-diameter single crystals of LLNbO. Therefore, growing of high-quality large diameter single crystals of LLNbO (x = 0.1) is so crucial and very appealing for all solid-state

battery application. Hence, we focused here to grow large diameter single crystals growth of LLNbO with LLNbO (x = 0.1) feed composition.

Recently, M. S. Ali *et. al.* [27] investigated the different conditions to grow the large diameter single crystals of LLNbO. They investigated that in heating zone area, lower temperature gradient in the upper portion caused smooth grown crystal in tilting-mirror furnace than that of conventional FZ furnace. They also investigated that the solid-liquid interface behavior for both furnaces. They optimized that the interface in the feed side for the conventional FZ furnace showed concave in shape whereas for tilting-mirror FZ furnace, the interface of the feed side was convex in shape and the convexity was larger with tilting-mirror angle θ = 10°. The large convexity was effective on crystal growth process and reduced the bobbles from molten zone easily during crystal growth process.

In the present study, crack- and inclusion-free, high-quality large-diameter single crystals of LLNbO (x = 0.1) have been grown using a tilting-mirror FZ furnace. Different conditions were imposed to determine the optimum growth conditions for high-quality single crystals. Furthermore, the mirror tilting effect on the large diameter single crystals growth of LLNbO has been investigated.

4. 2. Experimental Procedure

Li_2CO_3 (Rare Metallic Co., Ltd. 99.9%), La_2O_3 (Rare Metallic Co., Ltd. 99.9%) and Nb_2O_5 (Rare Metallic Co., Ltd. 99.9%) was used as starting raw materials, weighed to achieved a LLNbO (x = 0.10) stoichiometric composition and then mixed with ethanol. The mixed powder was dried and then calcined at 800 °C for 2 h in air atmosphere. The calcined powder was ground, grinded and again calcined at 1100 °C for 24 h in air atmosphere. The resulting powder was ground and grinded and then used for feed rod

preparation. The feed rods of approximately 11 mm in diameter and 50 mm in length were prepared by rubber pressing method under a hydrostatic pressure of 300 MPa and then sintered at 1150 ˚C to 1300 ˚C for 5 h in air or Ar atmosphere. Solvent of Li-rich (x = 0.185) and 10 mol% $LaNbO_4$-poor compositions relative to the stoichiometric composition of the LLNbO (x = 0.10) feeds was used for supporting the TSFZ growth.

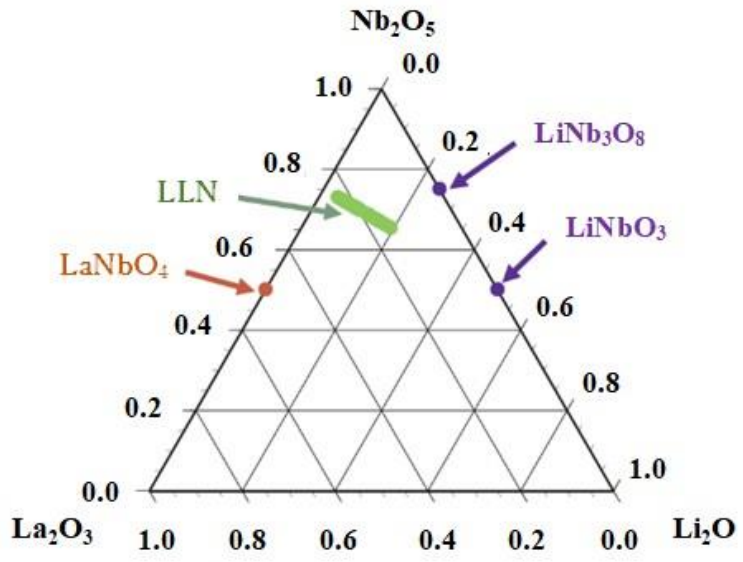

Fig. 4.4. Precipitated phases in La_2O_3-Li_2O-Nb_2O_5 system [22].

In **Fig. 4.4**, La_2O_3-Li_2O-Nb_2O_5 system phase diagram shows the incongruent-melting behavior of LLNbO [22]. LLNbO melts incongruently with $LaNbO_4$ and a liquid. Furthermore, the distribution coefficient of Li into the LLNbO solid solution was 0.54 which is than lower unity [20, 22]. Hence, solvent of Li-rich and 10 mol% $LaNbO_4$-poor composition relative to the stoichiometric composition of LLNbO feed composition was effective on not only the increase of Li concentration but also the suppression of $LaNbO_4$

phase in the LLNbO single crystals [20]. The solvent was prepared as the same procedure for feed rod preparation. About 1.2 g of solvent disk was used at the top of the feed rod of 11 mm in diameter.

The crystal growth was performed in an optical FZ machine (Crystal Systems Inc., model FZ-T-4000-H) and an image furnace with tilted mirrors (Crystal System Inc., model TLFZ-4000-H-VPO) with four 300 W halogen lamps. Schematic illustration of conventional and tilting-mirror FZ furnaces are shown in **Fig. 4.5**. In conventional FZ furnace, the mirror and heating lamps are aligned in the same horizontal plane. Besides, in tilting-mirror FZ furnace, the mirror and heating lamps are tilted from 0º to 20º by a motor drive control [28]. It was reported that the tilting angle θ of 10º is the best condition for crystal growth of $LiCoO_2$ [29] and large diameter LLNbO [27]. Hence, crystals growth of LLNbO was carried out at 0º - 10º to clarify the tilting angle effects as compared with conventional FZ furnace.

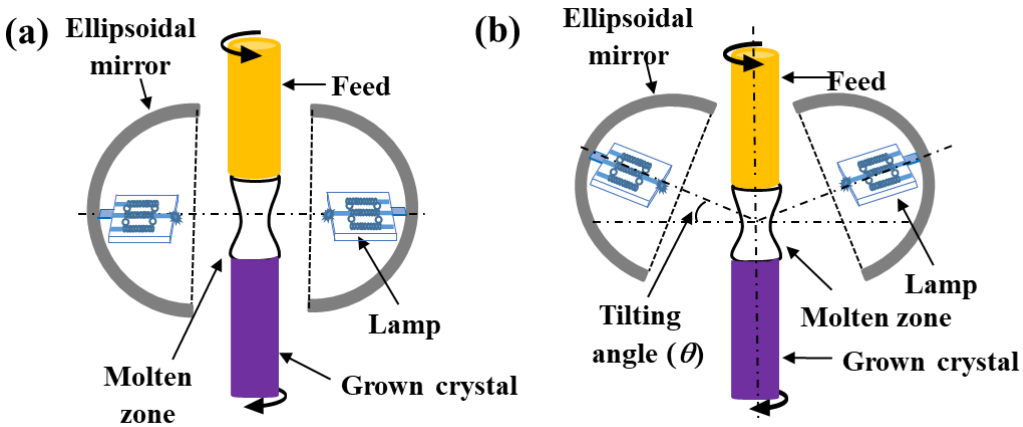

Fig. 4.5. Schematic illustration of (a) conventional FZ furnace and (b) tilting-mirror FZ furnace.

The growth rate was 5 mm/h with Ar (200 mL/min) atmosphere. Feed and seed rotation rates were 10 rpm and 30 rpm with opposite directions respectively. The grown crystals were then annealed with an O_2 atmosphere (50 mL/min) at 1000 °C for 24 h. The orientation of the seed and grown crystals was confirmed by the back-reflection Laue XRD (Rigaku Corp.) and two-dimensional XRD (Bruker Corp., model Discover D8 with a 2D detector). The crystal structure of the grown crystals was identified by X-ray diffraction method (XRD, Bruker Discover D8 with a 2D detector). XRD measurements were performed on cross-sections perpendicular to the growth direction of the O_2-annealed crystals without powdering. The identification of inclusion and composition of the grown crystals were analyzed by a scanning electron microscopy (SEM; Hitachi High-Tech, model TM-3030) with energy-dispersive X-ray spectroscopy (EDS; Bruker Corp., model Quantax70) and an electron probe microanalyzer (EPMA; JEOL Ltd., model JXA-iHP200F). The annealed crystals were cut and polished to a mirror surface, and then coated with carbon for SEM and EPMA analyses. The concentrations of La and Nb in the grown crystals were analyzed by EPMA quantitative analysis using the single crystals of $LaNbO_4$ as a standard sample. The Li concentration x in LLNbO crystals was calculated from the $Li_xLa_{(1-x)/3}NbO_3$ formula using the analytical values of La and Nb.

4.3. Results and Discussion

To grow high-quality large diameter single crystals of LLNbO, the optimum growth conditions were clarified. In the previous research work in our laboratory, it was reported that crack- and inclusion-free single crystals of LLNbO with 6 mm in diameter were grown using the solvent of Li-rich (x = 0.185) and 10 mol% $LaNbO_4$-poor compositions relative to the stoichiometric composition of the feed rods in TSFZ method [20]. Hence,

the large-diameter crystals of LLNbO were grown using the solvent of Li-rich ($x = 0.185$) and 10 mol% $LaNbO_4$-poor compositions relative to the stoichiometric composition of the feed rods. In these cases, we have used 1.2 gm solvent disk for approximately11 mm of feed rods. At first, we have tried to grow large-diameter single crystals of LLNbO using the conventional FZ furnace, however no crack-free crystals were observed. During crystal growth process, some small bubbles were formed and then coalesce into a larger one in the molten zone as shown in **Fig. 4.6**. When the large bubble was disappeared from the molten zone, then the molten zone became thin. For these, it was needed to move down the upper shaft very quickly otherwise melt was dropped very easily. However, contact problem occurred between feed rod and grown crystal in the molten zone during crystal growth process. As a result, the as-grown crystals contain many cracks. Also, the surface of the grown crystals was very rough (as shown in **Fig. 4.7**). The origin of bubble formation may be due to excess oxygen by reduction of Nb^{5+} in LLNbO feeds at a high temperature and air remaining in the porous feeds. Sintering at high temperatures (1300 °C) generally improves the sintering density of feed rods which reduced the bubbles problem from the molten zone during crystal growth process. However, Li was evaporated from the feed rods during at high sintering temperature. As a result, no cracks-free crystal was obtained using high sintering temperature. **Fig. 4.7** shows the photographs of as-grown crystal and crystal annealed in an O_2 atmosphere. The as-grown crystals exhibited black color and turned colorless and transparent after being annealed at 1000 °C for 24 h in an O_2 atmosphere. The as-grown crystals have oxygen deficiency and partial reduction of Nb^{5+} to Nb^{4+} by growth in Ar atmosphere. The oxygen deficiency and Nb^{4+} ions in Nb sites were suppressed by annealing in O_2 atmosphere. However, we changed the sintering atmosphere from air to Ar for bubbles reduction.

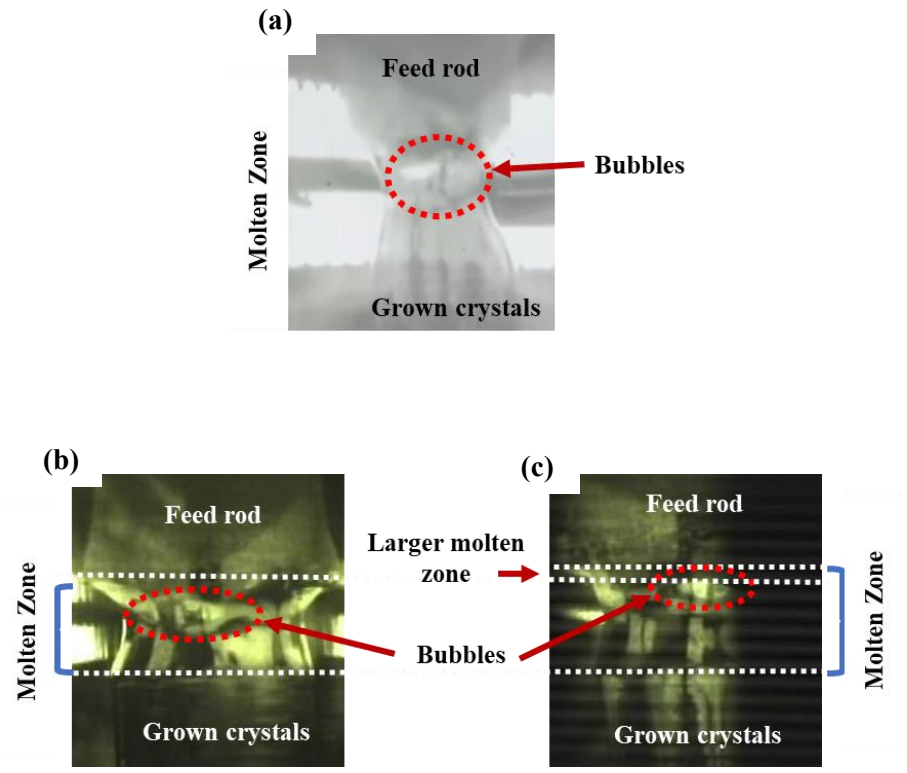

Fig. 4.6. Molten zone during crystal growth process using (a) conventional FZ furnace (b) tilting-mirror FZ furnace with $\theta = 0°$ and (C) tilting-mirror FZ furnace with $\theta = 10°$.

Unfortunately, same bubbles problems were occurred during crystal growth process. It was also reported that the growth atmosphere for Ar flow was strongly effective on reduction of bubble formation in the molten zone during TSFZ growth of LLNbO single crystals with 6 mm in diameter [20]. However, in the case of large-diameter single crystals of LLNbO, the bubble behavior in the molten zone was significantly influence on stability of the molten zone during TSFZ crystal growth process using the conventional FZ furnace even though under the optimum growth conditions in ref. 20. For the crystal growth using the conventional FZ furnace, the crystals shape was not uniform, and also the crystal contains many cracks. Cracking in the grown crystals is strongly related with instability

of the molten zone due to bubble behavior as well as contact problem in the molten zone during crystal growth process or Li-evaporation from feed rods during high temperature sintering.

(i) Sintering temperature of feed rod is 1200 °C.

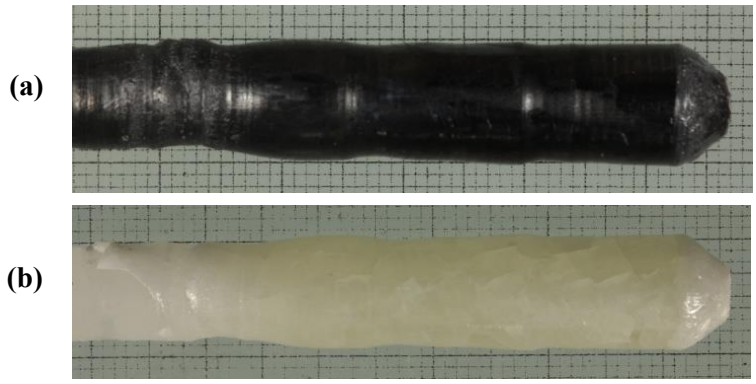

(ii) Sintering temperature of feed rod is 1300 °C.

Fig. 4.7. The as grown crystals of LLNbO using conventional FZ furnace (a) before annealing and (b) after annealing at O_2 atmosphere at 1000 °C for 24 h.

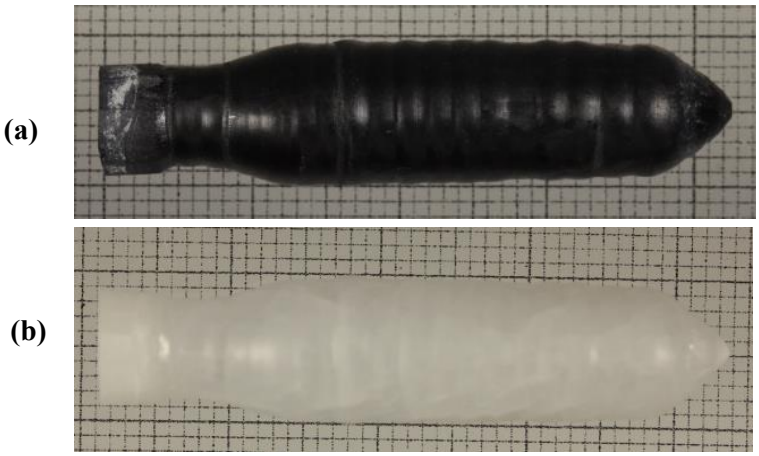

(i) Mirror tilting angle of $\theta = 0°$.

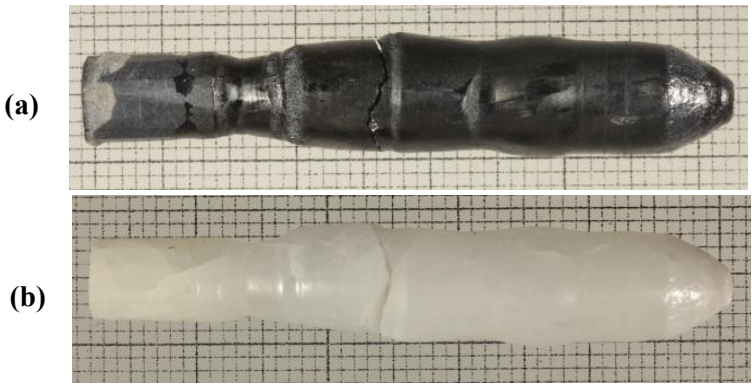

(ii) Mirror tilting angle of $\theta = 10°$.

Fig. 4.8. The as grown crystals of LLNbO using tilting-mirror FZ furnace (a) before annealing and (b) after annealing at O_2 atmosphere at 1000 °C for 24 h.

Therefore, to overcome the bubbles problem from molten zone during crystal growth process or Li-evaporation from feed rods during sintering, we tried to change the heating situation and the solid-liquid interface shape by using a tilting-mirror FZ furnace in order to remove bubbles from the molten zone. In the case of the tilting-mirror FZ furnace with tilting angle of $\theta = 0°$, some bubbles comparatively small in size were observed in the molten zone during crystals growth process. In addition, contact problem occurred

between feed rod and grown crystal in the molten zone during crystal growth process. As a result, molten zone was not stable for long time. On the other hand, when we changed to the tilting angle of $\theta = 10°$ from $\theta = 0°$, the molten zone height was larger than that of $\theta = 0°$ (**Fig. 4.6**). However, bubbles were also observed in the molten zone during crystal growth process. But the bubbles size was very small and removed easily from the molten zone may due to the high convexity in the feed-melt interface. Hence, bubble behavior was no effect on the grown crystal. In addition, no contact problem was occurred in this case. Hence, the molten zone was stable for a long time and the obtained grown crystals is almost cracks-free as shown in **Fig. 4.8.** The size of the grown crystals is about 30 mm in length and 9 mm in diameter. The growth direction of the grown crystals was determined to be [100] using the back-reflection Laue XRD and two-dimensional XRD.

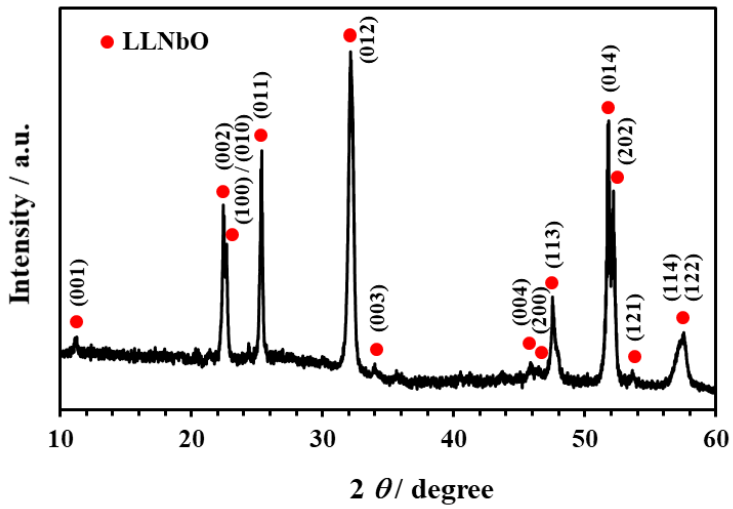

Fig. 4.9. XRD pattern of grown crystals.

Fig. 4.9 shows XRD pattern of the grown crystals. This XRD pattern is consistent with the previous reported data [18]. In particular, the (001) peak, which has about twice the

face spacing of (100) and (010), was observed, thereby confirming a double-perovskite structure.

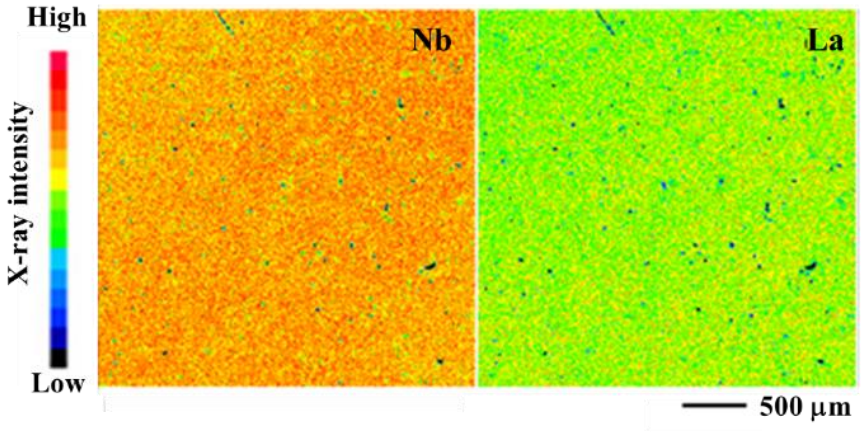

Fig. 4.10. Nb, La X-ray intensity distribution analyzed by EPMA.

The grown crystals of LLNbO were confirmed to be single crystals using EPMA analysis. **Fig. 4.10** shows the composition distribution in the middle part parallel to the growth direction of the grown crystal. No inclusions were found in the grown crystal. Many black spots in **Fig. 4.10** may be due to the voids in grown crystals or dust on the surface of the polished sample. The distribution of Nb and La shows the homogeneity of the LLNbO grown crystals. Also, the calculated values of La/Nb atomic ratio and Li concentration x are shown in **Table 4.1**. This table shows that the grown crystals using conventional FZ furnace contain low Li concentration than that of the grown crystals using tilting-mirror FZ furnace. However, the grown crystals using the tilting-mirror FZ furnace contain almost same Li concentration with both $\theta = 0°$ and $\theta = 10°$ mirror tilt angles. The Li concentration in the grown crystals is related with the required lamp power and Li evaporation from the molten zone during crystal growth. For crystal growth using the

conventional FZ furnace, higher lamp power was required. On the other hand, lower lamp power (almost same for both conditions, $\theta = 0°$ and $\theta = 10°$) was required during crystal growth using the tilting-mirror FZ furnace. Hence, comparatively higher amount of Li was evaporated during crystal growth process using the conventional FZ furnace than that of tilting-mirror FZ furnace. This was also confirmed by the amount of deposition of lithium compound inside the quartz tube during crystal growth process. Finally, we have confirmed that high-quality LLNbO single crystals with a diameter around 9 mm can be grown with good reproducibility using the tilting mirror FZ furnace at the tilting angle θ =10˚.

Table 4.1 Atomic concentration of LLNbO grown crystals

	FZ furnace	**Tilting-mirror FZ furnace**	
		($\theta = 0°$)	**($\theta = 10°$)**
La/Nb atomic ratio	0.309±0.001	0.308±0.001	0.308±0.001
Li concentration *x*	0.071±0.004	0.075±0.002	0.075±0.003

4.4. Conclusion

Large diameter single crystals of LLNbO has been grown under different conditions with Li-rich and 10%$LaNbO_4$-poor solvents using the TSFZ method. In conventional FZ furnace, the as-grown crystals contain many cracks due to high Li-evaporation and large bubbles in molten zone during crystal growth process. On the other hand, high-quality, homogeneous, and crack- and inclusion-free single crystals were grown using tilting-mirror FZ furnace with 10° tilted mirror condition. The as-grown crystals using tilting-mirror FZ furnace contain high Li concentration. Hence, low amount of Li was evaporated during crystal growth process using tilting-mirror FZ furnace than that of the conventional

FZ furnace. In addition, the reduction of bubbles from molten zone during crystal growth process using tilting-mirror FZ furnace with 10° tilted mirror angle is also effective to grow crack-free single crystals. Besides, the reduction of bubbles from molten zone during crystal growth process was observed with high sintering temperature but no crack-free crystals were obtained due to high Li evaporation during sintering. Hence, reproducible high-quality, homogeneous, and crack- and inclusion-free single crystals has been successfully grown using tilting-mirror FZ furnace with 10° tilted mirror condition. We hope that, the large-diameter single crystals of LLNbO may be applicable as a solid electrolyte for all solid-state Li-ion batteries. We are planning to use our grown LLNbO crystals in solid-state Li-ion batteries.

References

1) J. -M. Tarascon and M. Armand, *Nature* **414** 359 (2001).

2) A. S. Arico, P. Bruce, B. Scrosati, J.-M. Tarascon and W. Van Schalkwijk, *Nat. Mater.* **4** 366 (2005).

3) M. Armand and J.-M. Tarascon, *Nature* **451** 652 (2008).

4) P. G. Bruce, B. Scrosati, and J.-M. Tarascon, *Angew. Chem. Int. Ed.* **47** 2930 (2008).

5) J. B. Goodenough and Y. Kim, *Chem. Mater.* **22** 587 (2010).

6) V. Etacheri, R. Marom, R. Elazari, G. Salitra and D. Aurbach, *Energy Environ. Sci.* **4** 3243 (2011).

7) B. Dunn, H. Kamath and J. -M. Tarascon, *Science* **334** 928 (2011).

8) N. Nitta, F. Wu, J.T. Lee and G. Yushin, *Mater. Today* **18**, 252 (2015).

9) J. W. Choi and D. Aurbach, *Nat*. *Rev*. *Mater*. **1** 16013 (2016).

10) N. Kamaya, K. Homma, Y. Yamakawa, M. Hirayama, R. Kanno, M. Yonemura, T. Kamiyama, Y. Kato, S. Hama, K. Kawamoto and A. Mitsui, *Nat. Mater.* **10** 682 (2011).

11) F. Aguesse, V. Roddatis, J. Roqueta, P. Garcia, D. Pergolesi, J. Santiso and J. A. Kilner, *Solid State Ionics* **272** 1 (2015).

12) D. Rettenwander, R. Wagner, J. Langer, M. E. Maier, M. Wilkening and G. Amthauer, *Eur. J. Mineral.* **28** 619 (2016).

13) K. Kataoka, H. Nagata and J. Akimoto, *Sci. Rep.* **8** 9965 (2018).

14) S. Minegishi, T. Hoshina, T. Tsurumi, K. Lebbou and H. Takeda, *J. Ceram. Soc. Jpn.* **128** 481 (2020).

15) M. A. R. Sarker, S. Watauchi, M. Nagao, M. M. Hossain and I. Tanaka, *J. Phys.: Conf. Ser*. **1718** 012012 (2021).

16) A. E. D. Barr, *Contemp. Phys.* **2** 409 (1961).

17) Milisavljevic and Y. Wu, *BMC Mat.* **2** 2 (2020).

18) Y. Fujiwara, K. Hoshikawa and K. Kohama, *J. Cryst. Growth* **433** 48 (2016).

19) Y. Fujiwara, T. Taishi, K. Hoshikawa, K. Kohama and H. Iba, *Jpn. J. App. Phys.* **55** 090306 (2016).

20) M. S. Ali, N. Sato, I. Fukasawa, Y. Maruyama, M. Nagao, S. Watauchi and I. Tanaka, *Cryst. Growth Des.* **19** 6291 (2019).

21) M. S. Ali, Y. Maruyama, M. Nagao, S. Watauchi and I. Tanaka, *Solid Sate Ionics* **350** 115330 (2020).

22) I. Tanaka, R. Yoshihara, C. Nakazawa, M. Nagao and S. Watauchi, *J. Cryst. Growth*, **507** 251 (2019).

23) N. Kamaya, K. Homma, Y. Yamakawa, M. Hirayama, R. Kanno, M. Yonemura, T. Kamiyama, Y. Kato, S. Hama, K. Kawamoto and A. Mitsui, *Nature materials* **10** 682 (2011).

24) S. Komura and I. Shindo, *J. Cryst. Growth* **41(2)** 192 (1977).

25) I. Tanaka and H. Kojima, *Nature* **337** 21 (1989).

26) I. Tanaka, K. Yamane and H. Kojima, *J. Cryst. Growth* **96** 711 (1989).

27) M. S. Ali, Ph.D. Dissertation, Interdisciplinary Graduate School of Medicine, Engineering and Agriculture Sciences, University of Yamanashi (2020).

28) S. Nakamura, A. Maljuk, Y. Maruyama, M. Nagao, S. Watauchi, T. Hayashi, Y. Anzai, Y. Furukawa, C. D. Ling, G. Deng, M. Avdeev, B. Buchner and I. Tanaka, *Cryst. Growth Des.*, **19(1)** 415 (2019).

29) R. Parvin, Y. Maruyama, M. Nagao, S. Watauchi and I. Tanaka, *Cryst. Growth Des.* **20(5)** 3413 (2020).

Chapter 5

Social impact and business potential of my research

5.1. Social impact and business potential of my research

My present research is directly related to social feasibility, industrial application and contribution to the global economy. Since, the uses of rechargeable lithium-ion batteries (LIBs) as continuous power sources are increased day by day due to their various application sectors including portable electronic devices, electric/hybrid electric vehicles, marine vehicles, autonomous aircraft, smart grids, solar power storage systems, robots etc. [1-9]. For example, the expected global annual demand of LIBs for electric mobility applications is to increase from 10 GWh in 2015 to almost 1300 GWh in 2030 [10]. In addition, the global battery demand from 2020 to 2030 for transportation, stationary and consumer electronics are shown graphically in **Fig. 5.1.**

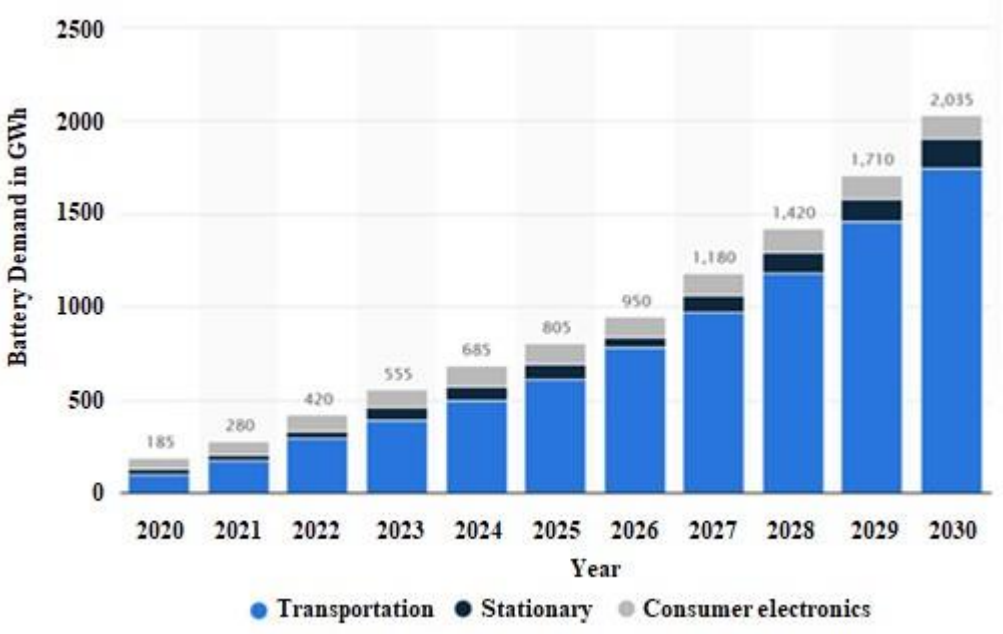

Fig. 5.1. Global battery demand from 2020 to 2030, by application [11].

So, high performing LIBs is very important for the next generation. In most of the commercial LIBs, organic liquid electrolytes or polymer-based electrolytes are used. The ionic conductivity of the organic electrolytes is high about (10^{-2} S cm $^{-1}$) which ensures the rapid ion movements, good battery performances, and decent rate performances of LIBs. But organic or polymer electrolytes may possess dendrite formation, leakage, short circuit and flammability problems in LIBs. For example, in 2013 a Japan airline 787 Dreamliner's cargo and in 2016 Samsung's Galaxy note 7 catching on fire [12-14]. This firing problems might be occurred due to dendrite problems from anode to cathode which caused short circuit in LIBs. To overcome these issues, it is urgent needed to replace the liquid electrolytes by solid electrolyte for all solid-state LIBs [15]. Now a days, research on inorganic solid electrolytes have attracted enormous attention for developing all solid-state LIBs due to their various advantages including absolute safety, no issues of leakages of toxic organic solvents, low flammability, non-volatility and higher cyclability [16]. For example, more than 20 world largest companies including Toyota, Toshiba, Honda, BMW, Nissan, Fisker, Panasonic, Samsung, CATL and so on are involved for developing the solid-state LIBs [17].

However, polymer based solid electrolytes or poly crystalline solid electrolytes contain grain boundary which may causes dendrite formation from anode to cathode and then create short circuits between electrodes in LIBs [16,18-21]. On the other hand, some inorganic solid electrolytes such as sulfides, glasses or oxides may expected as electrolytes for the next generation LIBs. Glasses and sulfides have high ionic conductivity but these are air exposure and produce environmentally toxic hydrogen sulfide. In addition, solid sulfides may react with lithium metal anode and cause short circuit problem in LIBs [22-27]. Compared to other electrolytes, oxide based single

crystals of solid electrolytes are environmentally safe in use but these possess typically low ionic conductivity. In single crystals of solid electrolyte, here is no grain boundary. Hence, the there is no chance of dendrite formation from anode to cathode through single crystals of solid electrolytes in solid-state LIBs. In addition, single crystal of solid electrolyte with layered structure possess the anisotropic ionic conductivity. So, high anisotropic Li-ion conducting single crystal of solid electrolyte will increase the performance, lifetime and safety issues of all solid-state LIBs.

In order to meet the demand for solid-state LIBs over the next generations, new materials for single crystals of solid electrolytes must be introduced. Researchers are attempting to use single crystals of solid electrolytes in solid-state LIBs. However, investigation of solid electrolytes with high ionic conductivity, environmentally safe in use, and low in cost is quite difficult for the researchers. My present research is closely related to future development of all solid-state LIBs. This research significantly influences both industrial applications and social developments. I hope that my investigation results on the solid electrolytes may have a significant impact on the worldwide technology revolution for the next generations LIBs.

References

1) J. -M. Tarascon and M. Armand, *Nature* **414** 359 (2001).
2) A. S. Arico, P. Bruce, B. Scrosati, J.-M. Tarascon and W. Van Schalkwijk, *Nat. Mater.* **4** 366 (2005).
3) M. Armand and J.-M. Tarascon, *Nature* **451** 652 (2008).
4) P. G. Bruce, B. Scrosati, and J.-M. Tarascon, *Angew. Chem. Int. Ed.* **47** 2930 (2008).
5) J. B. Goodenough and Y. Kim, *Chem. Mater.* **22** 587 (2010).
6) V. Etacheri, R. Marom, R. Elazari, G. Salitra and D. Aurbach, *Energy Environ. Sci.* **4** 3243 (2011).
7) B. Dunn, H. Kamath and J.-M. Tarascon, *Science* **334** 928 (2011).
8) N. Nitta, F. Wu, J.T. Lee and G. Yushin, *Mater. Today* **18** 252 (2015).
9) J. W. Choi and D. Aurbach, *Nat. Rev. Mater.* **1** 16013 (2016).
10) C. Thiesa, K. Kieckhafera, T. S. Spenglera and M. S. Sodhib, *Procedia CIRP* **80** 292 (2019).
11) https://www.statista.com/statistics/1103218/ (2023).
12) "Dreamliner: Boeing 787 planes grounded on safety fears" BBC News, January 17, 2013.
13) A. Burning, *Chem. Eng. News* **94 (45)** 33 (2016).
14) S. Boyford, Samsungs says bad batteries and rushed manufacturing doomed the Galaxy Note 7, January 22, 2017.
15) Y. Kato, S. Hori, T. Saito, K. Suzuki, M. Hirayama, A. Mitsui, M. Yonemura, H. Iba, and R. Kanno, *Nature Energy* **3** 438 (2016).
16) Z. Chena, G.-T. Kima, Z. Wangd, D. Bressera, B. Qina, D. Geigere, U. Kaisere, X Wangd, Z. X. Shenc, S. Passerini, *Nano Energy* **64** 103986 (2019).

17) X. He, idtechhex.com. “The market size of solid state batteries will reach $6 billion by 2030” July 2020, slides 336.

18) M. R. Reisch, *Chem. Eng. News* **95 (46)** 19 (2017).

19) Y. Xiayin, H. Bingxin, Y. Jingyun, P. Gang, H. Zhen, G. Chao, L. Deng and X. Xiaoxiong, *Chinese Physics B* **25(1)** 018802 (2016).

20) A. Vandervell (26 September 2017). “What is a solid-state battery? The benefits explained”. Wired UK.

21) C. Sun, J. Liu, Y. Gong, D. P. Wilkinson and J. Zhang, *Nano Energy* **33** 363 (2017).

22) N. Kamaya, K. Homma, Y. Yamakawa, M. Hirayama, R. Kanno, M. Yonemura, T. Kamiyama, Y. Kato, S. Hama, K. Kawamoto and A. Mitsui, *Nat. Mater.* **10** 682 (2011).

23) F. Aguesse, V. Roddatis, J. Roqueta, P. Garcia, D. Pergolesi, J. Santiso and J. A. Kilner, *Solid State Ionics* **272** 1 (2015).

24) D. Rettenwander, R. Wagner, J. Langer, M. E. Maier, M. Wilkening and G. Amthauer, *Eur. J. Mineral.* **28** 619 (2016).

25) K. Kataoka, H. Nagata and J. Akimoto, *Sci. Rep.* **8** 9965 (2018).

26) S. Minegishi, T. Hoshina, T. Tsurumi, K. Lebbou and H. Takeda, *J. Ceram. Soc. Jpn.* **128** 481 (2020).

27) M. A. R. Sarker, S. Watauchi, M. Nagao, M. M. Hossain and I. Tanaka, *J. Phys.: Conf. Ser*. **1718** 012012 (2021).

Chapter 6

Summary and prospects of my research

6.1. Summary

Unwanted climate change and environmental degradation is one of the greatest challenges to humankind. Lithium-ion battery (LIB) plays an important role in the demand for green and sustainable energy. But some issues arise in the present LIBs including firing and explosion problems. These problems may be causes due to dendrite formation from anode to cathode through liquid or polymer electrolytes which causes short circuit in LIBs. Researcher are trying to overcome these problems. Replacement of liquid or polymer electrolytes by other suitable electrolyte to solve these problems is big challenges for the researchers. Some inorganic solid electrolytes such as sulfides, glasses or oxides may expected as electrolytes for the next generation LIBs. Glasses and sulfides have high ionic conductivity but these are air exposure and produce environmentally toxic hydrogen sulfide. However, solid sulfides may react with lithium metal and cause short circuit problem in LIBs. In addition, poly crystalline solid electrolytes contain grain boundary which may causes dendrite formation. In contrast, single crystal of oxide solid electrolytes with layered structure possess the anisotropic ionic conductivity, and also there is no chance of dendrite formation. So, high anisotropic Li-ion conducting single crystal of solid electrolyte will increase the performance, lifetime and safety issues of all solid-state LIBs.

$Li_{3x}La_{2/3-x}TiO_3$ (LLTiO) with double-perovskite structure has high ionic conductivity (10^{-3} $S \cdot cm^{-1}$ at room temperature). However, Ti^{4+} can be easily reduced by Li-metal anodes, producing Ti^{3+} in higher-capacity LIBs. In contrast, Nb^{5+} and Ta^{5+} is resistant to reduction

by Li-metal anode. Therefore, $Li_xLa_{(1-x)/3}TaO_3$ (LLTaO) and $Li_xLa_{(1-x)/3}NbO_3$ (LLNbO) with a double-perovskite structure is a desirable solid electrolyte candidate for investigating high-capacity LIBs. In this study, we have grown LLTaO and LLNbO single crystals using traveling solvent floating zone (TSFZ) method. Then we have characterized the grown crystals.

This dissertation is consisted of six chapters. The summary is as follows:

In ***Chapter 1***, I have described about LIBs and why we need solid-state LIBs. Then I have described solid electrolytes and its classification. Finally, I have described my purpose of research.

In ***Chapter 2***, I have described the methodology of this research. Here, I have described the crystal growth techniques and instruments. Then I have described the characterization techniques of the grown crystals.

In ***Chapter 3***, I have discussed about the single crystal growth of $Li_xLa_{(1-x)/3}TaO_3$ (LLTaO) with lithium concentration $x = 0.18$ due to its high ionic conductivity. At first, we have tried to grow single crystals of LLTaO using FZ method. Due to incongruent melting behavior of LLTaO, no inclusion free single crystals were found in FZ method. Inclusion- and crack-free transparent bulk single crystals of LLTaO were successfully grown using the TSFZ growth method in a Ta-poor solvent (8% $LiTa_3O_8$-poor composition from LLTaO) in the Ar atmosphere. The grown crystals exhibited black color due to oxygen deficiency in the growth atmosphere. When the crystals were left overnight in the air at room temperature, they became colorless and transparent. This phenomenon suggests that oxygen diffusion is rapid even at room temperature, which is very interesting not only in the aspect of lithium ion conduction but also in oxygen conduction. The LLTaO crystals grown using the feeds of $x = 0.18$ showed a uniform Li concentration

of 0.086 ± 0.001, which was lower than that of the feed because of the Li-poor solvent and Li evaporation during crystal growth. The anisotropic ionic conductivities of the grown crystals were determined to be $\sigma_{[110]} = 2.8 \times 10^{-5}$ S·cm^{-1} and $\sigma_{[001]} = 1.8 \times 10^{-5}$ S·cm^{-1}. Therefore, the Li^+ mobility perpendicular to the *c*-axis is higher than that parallel to the *c*-axis, indicating that the LLTaO single crystals oriented parallel to the *c*-axis are desirable substrates for producing next-generation solid-state Li-ion batteries. To characterize the electrochemical properties of LLTaO, we prepared the UFO cells using LLTaO single crystals as solid electrolyte. But no operation was observed may due to the short circuit or internal high resistance of the cells.

In ***Chapter 4,*** I have discussed about the large diameter single crystal growth of $Li_xLa_{(1-x)/3}NbO_3$ (LLNbO) with lithium concentration $x = 0.10$ due to its high ionic conductivity. Large diameters single crystals of LLNbO has been grown under different conditions with Li-rich and 10%$LaNbO_4$-poor solvents using the TSFZ method. In conventional FZ furnace, the as-grown crystals contain many cracks due to high Li-evaporation and large bubbles in molten zone during crystal growth process. On the other hand, high-quality, homogeneous, and crack- and inclusion-free single crystals were grown using tilting-mirror FZ furnace with 10° tilted mirror condition. The as-grown crystals using tilting-mirror FZ furnace contain high Li concentration. Hence, low amount of Li was evaporated during crystal growth process using tilting-mirror FZ furnace than that of the conventional FZ furnace. In addition, the reduction of bubbles from molten zone during crystal growth process using tilting-mirror FZ furnace with 10° tilted mirror angle is also effective to grow crack-free single crystals. Besides, the reduction of bubbles from molten zone during crystal growth process was observed with high sintering temperature but no crack-free crystals were obtained due to high Li evaporation during

sintering. Hence, reproducible high-quality, homogeneous, and crack- and inclusion-free single crystals has been successfully grown using tilting-mirror FZ furnace with 10° tilted mirror condition. We hope that, the large-diameter single crystals of LLNbO may be applicable as a solid electrolyte for all solid-state Li-ion batteries. We are planning to use our grown LLNbO crystals in solid-state Li-ion batteries.

In *Chapter 5*, I have explained the social impact and business potential of my research.

In *Chapter 6*, I have summarized and described the prospects of my research.

6.2. Prospects

Lithium-ion batteries (LIBs) are widely used as continuous power sources for portable electronic devices, electric/hybrid electric vehicles, marine vehicles, autonomous aircraft, smart grids, solar power storage systems, robots etc. So, developments of LIBs have become a hot spot in the research area for next generation energy storage devices. Single crystals of double-perovskite oxide solid electrolytes have received tremendous attention over the liquid electrolytes or others solid electrolytes due to their various advantages including high anisotropic ionic conductivity, no grain boundary, no dislocation of atoms, excellent mechanical stability and higher energy density. Hence, there is no chance of overheating and dendrite formations in LIBs by replacing single crystals of solid electrolytes instead of organic liquid or polymer based solid electrolyte or polycrystalline solid electrolyte. In this research work, we have study on single crystals of double-perovskite $Li_xLa_{(1-x)/3}TaO_3$ (LLTaO) and $Li_xLa_{(1-x)/3}NbO_3$ (LLNbO). We have successfully grown these single crystals using TSFZ method. We have investigated the anisotropic ionic conductivity of LLTaO single crystals. We have also grown the large diameter single crystals of LLNbO for LIBs applications. We hope that these investigation results may

present a new opportunity for the researcher to utilize single crystals of solid electrolyte for all solid-state LIBs.

APPENDIX

Papers published in reviewed Journals

1. **Most. Umme Salma**, Yuki Maruyama, Masanori Nagao, Satoshi Watauchi, Hirokazu Munakata, Kiyoshi Kanamura and Isao Tanaka, "TSFZ growth and anisotropic ionic conductivity of $Li_xLa_{(1-x)/3}TaO_3$ single crystals", *Journal of the Ceramic Society of Japan* **131 [4]** 72-76 (2023).
2. **Most. Umme Salma**, Md. Shahajan Ali, Yuki Maruyama, Masanori Nagao, Satoshi Watauchi and Isao Tanaka, "Growth of Large-diameter $Li_xLa_{(1-x)/3}NbO_3$ Single Crystal by the TSFZ method using a tilting-mirror FZ furnace", *Journal of Flux Growth* **17 [1]** 7-11 (2023).

Conference presentations (Oral presentations):

1. **Most Umme Salma**, Yuki Maruyuma, Masanori Nagao, Satoshi Watauchi, Isao Tanaka, "TSFZ Growth and Characterization of $Li_xLa_{(1-x)/3}TaO_3$ Single Crystals"; *The 15th Conference of The Flux Growth Society of Japan*, 2-3 December 2021, Shinshu University, Japan.
2. **Most. Umme Salma**, Yuki Maruyuma, Masanori Nagao, Satoshi Watauchi, Isao Tanaka, "TSFZ growth and anisotropic ionic conductivity of $Li_xLa_{(1-x)/3}TaO_3$ single crystals", *IUMRS-ICYRAM 2022 (The 5th International Union of Materials Research Societies; International Conference of Young Researchers on Advanced Materials)*, 3-6 August 2022, Kyushu University, Japan.

Acknowledgments

All praise for Allah who has created us and given a greatest status among his all creations. I also express my gratefulness to the creator Allah to give me strength, courage, patience and ability to complete this study. I am also greatly thankful to my dearest parents for their profound support.

I would like to express my deepest sense of gratitude to my honorable supervisors Professor Nobuhiro Kumada and Professor Isao Tanaka, Center for Crystal Science and Technology, University of Yamanashi, Japan, for their scholastic supervision, valuable guidance and helpful discussion throughout the progress of this work. I am highly grateful to them for allowing me to pursuing this study under their supervision.

I am deeply grateful to Professor Kiyoshi Kanamura and Professor Hirokazu Munakata for supervising me during my internship collaboration research work, Department of Applied Chemistry, Tokyo Metropolitan University, Japan. Also, I would like to thank to Ms. Mayuko Kobayashi for her cordial co-operation.

I also would like to cordial thanks to Professor Yuki Maruyama, Professor Satochi Watauchi and Professor Masanori Nagao for their insightful comments and encouragement, especially continuous technical help to accomplish this research smoothly.

Special thanks to Professor Takahiro Takei, Professor Keisuke Arimoto, Professor Kosuke Hara, Professor Junji Yamanaka, Professor Yoshinori Yonesaki, Professor Norio Saito and who provided me an opportunity to access the laboratory and research facilities.

I am also thankful to the all officials staff affiliated with Center for Crystal Science and Technology and Office of International affairs, University of Yamanashi for their co-

operation. In particularly, I am grateful to Ms. Nozomi, Ms. Hashizume and Ms. Watanabe for their continuous support inside and outside the laboratory issues. I am greatly thankful to all the students of this laboratory for their helpful behavior. I am especially thankful to Mr. Ali, Mr. Riju, Ms. Ruma, Mr. Okanda and Mr. Yoshida for their instrumental help during my study.

I would like to extend my thanks those authors who I have mentioned and those I have not mentioned for their informative papers and materials related to this study.

I am very much grateful to my family members, teachers, friends and well-wishers for their encouragement and moral supports.

I want to express my special thanks to the Japanese Government; Ministry of Education, Culture, Sports, Science and Technology (MEXT) for providing me JASSO scholarship for six months. Finally, I would like to express my thanks to Green Energy Conversion Science and Technology and Power Energy Professional (PEP) program for their financial support during time PhD study.

The Author

Most. Umme Salma

September 2023